Research Article Vol. 3, No. 8 / 15 August 2020 / OSA Continuum 2106

Parametric study of optical transmission through plasmonic hole arrays modulated by the phase transition of vanadium dioxide

EUGENII U. DONEV,[1,3,*] FRANCIS X. HART,[1] BERTRAND IRAKOZE NKURUNZIZA,[1,4] KEVIN BERTSCHINGER,[2] JINLIN ZHANG,[2] AND JAE YONG SUH[2]

[1]Department of Physics and Astronomy, The University of the South, Sewanee, TN 37383, USA
[2]Department of Physics, Michigan Technological University, Houghton, MI 49931, USA
[3]Currently with the Department of Physics, Engineering and Astronomy, Austin Peay State University, P.O. Box 4608, Clarksville, TN 37044, USA
[4]Currently with SAF-HOLLAND, Muskegon, MI 49442, USA
[*]edonev@gmail.com

Abstract: We have performed comprehensive electromagnetic simulations and preliminary experiments to explore the effects of geometrical and material parameters on the extraordinary optical transmission (EOT) through periodic arrays of subwavelength holes in a bilayer stack consisting of a gold or silver film atop a vanadium dioxide film (Au/Ag + VO_2), where the latter undergoes a semiconductor-to-metal phase transition. Using the finite-difference time-domain (FDTD) and finite-element methods (FEM), we vary iteratively the array periodicity, VO_2 film thickness and hole diameters, as well as the refractive index inside the VO_2-layer holes and the VO_2 optical constants. For each variation, we compare the metallic-to-semiconducting ratios of the zero-order transmission (T_{00}) peaks and find sharp maxima in these ratios within narrow parameter ranges. The maxima arise from Fabry-Perot and Fano-type resonances that minimize T_{00} in the semiconducting phase of the perforated bilayers. At a fixed array period, the primary factors controlling the VO_2-enabled EOT modulation are the VO_2 thickness, diameter of the VO_2-layer holes, and absorption in the two VO_2 phases. Besides uncovering the origins of the higher metallic-phase T_{00}, this study provides a protocol for optimizing the performance of the bilayer hole arrays for potential uses as dynamically tunable nano-optical devices.

1. Introduction

Transmission of light through narrow apertures is one of the paradigms of nanoscale optics [1–5]. Unforeseen by standard diffraction theory [6,7], the so-called extraordinary or enhanced optical transmission (EOT) [8–10] manifests itself as a sequence of sharp dips and asymmetric peaks in the far-field spectra of electromagnetic waves transmitted through arrays of subwavelength apertures in metallic films. The current understanding of EOT through nanohole arrays [9,11,12] attributes the primary transmission mechanism to resonant tunneling [13] of evanescent modes boosted by multiple scattering of hybrid waves consisting of surface-plasmon polaritons [14] and quasi-cylindrical [15] or Norton [16] surface waves. Hole arrays have found many uses [5,10,17]—for example, in sensing [18,19], nanochemistry [20], plasmonic nano-tweezers [21], optofluidics [22], thermoplasmonics [23], surface-enhanced Raman spectroscopy [24–26], plasmonic color generation and control [27,28], surface-plasmon lasing [29], and tunable optical devices [30]. For subwavelength apertures, several methods have been devised for active modulation of the transmission, generally by altering the optical constants of the adjacent materials via external stimuli: photoinduced [31–35], magnetic [36,37], electrical [38], electronic [39–41], electrochemical [42], electrochromic [43], and thermochromic [44–47]. The latter is

#390879 https://doi.org/10.1364/OSAC.390879
Journal © 2020 Received 2 Mar 2020; revised 29 Apr 2020; accepted 21 May 2020; published 5 Aug 2020

OSA CONTINUUM

the focus of this paper, which systematically investigates the modulation of the EOT effect by means of a reversible, temperature-induced, semiconductor-to-metal phase transition (SMPT).

The paper describes the parameters that affect the EOT switching for bilayer hole-array nanostructures comprising a plasmonic metal (gold, Au, or silver, Ag) and thermochromic vanadium dioxide (VO_2). Section 2 presents preliminary experimental results for gold + VO_2 bilayer hole arrays of periodicities 650 nm and 845 nm. Section 3 introduces the numerical and analytical methods employed in this work and maps out the parameter space explored via electromagnetic simulations. Section 4 presents simulations results for zero-order optical transmission (T_{00}) peaks, ratios, and spectra for variations in geometrical and materials parameters: Au + VO_2 array period, VO_2-layer thickness, Au + VO_2 thru-hole diameter, VO_2-hole diameter, VO_2 absorption, VO_2-hole refractive index, VO_2 complex refractive index, Ag + VO_2 array period with and without VO_2 holes, and Ag + VO_2 thru-hole diameter. Section 5 includes image plots of simulated power flow and electric-field intensity in some representative scenarios: unperforated vs. perforated VO_2 layer, three VO_2-hole diameters, two VO_2-layer thicknesses, and three Au + VO_2 array periods. Section 6 summarizes our findings. Supplement 1 includes some of the details, figures, and discussions.

Our method of modulating the optical transmission through plasmonic nanohole arrays utilizes vanadium dioxide, a canonical correlated-electron material that undergoes phase transitions driven by temperature or light [48–50]. Above a critical temperature $T_{crit} = 340$ K (67 °C), bulk VO_2 switches from a monoclinic semiconductor to a rutile metal, and vice versa upon cooling. These coupled electronic and structural phase transitions are typically manifested by hysteresis loops in the electrical, crystallographic and optical properties of the VO_2 sample as a function of temperature; for example, see the transmittance measurement in Fig. 1(a). A planar, undecorated VO_2 film is more opaque to infrared (IR) light in the metallic (MetVO_2, $T > T_{crit}$) than in the semiconducting (SemiVO_2, $T < T_{crit}$) state and the contrast increases at longer wavelengths, as shown by the calculated transmittance in Fig. 1(b). The relative permittivity [Fig. 1(c, d)] and index of refraction [Fig. 1(e, f)] have non-negligible imaginary components, exhibit significant dispersion (esp. for MetVO_2) and differ substantially in the two states. It is these large changes in optical constants, induced close to room temperature during the SMPT, that make VO_2 a prime candidate for (ultrafast [51]) tunable optoelectronic devices. Examples of VO_2-enabled plasmonic modulators and switches can be found in Refs. [47,52–59].

In principle, the EOT effect can be tuned across the SMPT by dwelling at different sample temperatures in the transition regions where the optical constants of VO_2 change continuously from their SemiVO_2 to MetVO_2 values on heating and vice versa on cooling [60,61]. The hysteresis enables bistable switching for thermal excursions of 15 °C or more in the two end states, while within the hysteresis loop the EOT magnitude depends on whether a given temperature is reached by ramping up or down. These latter scenarios are beyond the scope of the current work, for which we performed optical measurements first at room temperature (SemiVO_2) and then at a stable 85 °C (MetVO_2). Since the VO_2 phase transition is fully reversible, the order of the final-state measurements does not affect the switching functionality.

We have performed three-dimensional electromagnetic simulations and preliminary experiments, aiming to optimize the structural parameters of bilayer nanohole arrays in a gold (Au) or silver (Ag) film atop a VO_2 film on a semi-infinite glass substrate ($n_{glass} = 1.50$; see inset in Fig. 3) or freestanding in air ($n_{air} = 1.00$), for potential applications in nanoplasmonic optical switching. We obtain closely matching computational results with two different fully vectorial Maxwell solvers. As we vary the geometry of the perforated Au + VO_2 or Ag + VO_2 bilayers, we search the parameter space for combinations of array period, hole diameter and VO_2 film thickness that *maximize the ratio of the zero-order transmission at the longest-wavelength EOT peak in the MetVO_2 state, peak-T_{00}, to the zero-order transmission at the same wavelength in the SemiVO_2 state*. For the remainder of this paper, we refer to this Met-to-Semi peak-T_{00} ratio,

OSA CONTINUUM

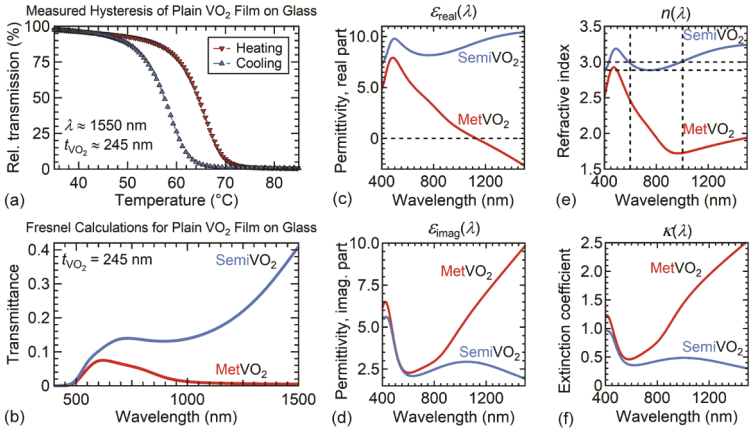

Fig. 1. Vanadium dioxide (VO_2) undergoes abrupt, reversible, thermally induced semiconductor-to-metal phase transition (SMPT). **(a)** Transmission of 1550-nm light, normalized to maximum value at 25 °C, as a function of temperature for plain (i.e., unperforated) 245-nm-thick VO_2 film on glass substrate. Steepness, contrast, width and critical temperatures of hysteresis loop signify high-quality sample. **(b)** Transmittance through plain 245-nm-thick VO_2 film on glass, calculated with Fresnel equations using frequency dispersions of **(c)** real and **(d)** imaginary parts of relative permittivity $\varepsilon(\lambda)$ or, equivalently, **(e)** refractive index $n(\lambda)$ and **(f)** extinction coefficient $\kappa(\lambda)$ of VO_2. These optical constants were obtained from FDTD software fits to experimental data extracted from Ref. [59]. The pronounced changes in optical constants across the SMPT underpin the functionality of VO_2 as a modulator of EOT through nanohole arrays in plasmonic metals.

which quantifies the EOT switching or modulation, as the *M2S-ratio*. After several iterative optimizations, the simulations of gold + VO_2 hole arrays on glass (i.e., Air-Au + VO_2-Glass) produced a maximum M2S-ratio = 188 at a peak wavelength λ_{peak} = 778 nm with these optimal parameters: array period P_{array} = 720 nm, thru-hole diameter $D_{thru-hole}$ = 302 nm, and combined Au and VO_2 bilayer thickness t_{Au+VO2} = 200 + 245 nm.

Furthermore, we seek to elucidate the electromagnetic origins of the effect we term *reverse optical switching*, observed in the current experiments and simulations [e.g., Fig. 3(a)] and previously in Refs. [44,62], whereby the EOT through Au + VO_2 and Ag + VO_2 bilayer hole arrays is counterintuitively higher in the MetVO_2 state than in the SemiVO_2 state. Such increase in light transmission through a perforated VO_2 film across the SMPT is 'reverse' in the sense that 'ordinary' IR transmission through a plain (unperforated) VO_2 film is lower in the metallic state [e.g., Fig. 1(a, b)].

We find the highest M2S-ratios occur when transmission at λ_{peak} through the perforated Au + *Semi*VO_2 bilayer decreases sharply within narrow ranges of the explored parameters—array period, VO_2 film thickness, thru-hole diameter, VO_2-hole diameter and VO_2 absorption —while the corresponding peak-T_{00} for Au + *Met*VO_2 follows a monotonic trend for all but one parameter sweeps. When varying VO_2 thickness or hole diameter, the dips in peak-T_{00} for Au + SemiVO_2 likely originate from Fabry-Perot (FP) resonances [4,9,63–65] that build up standing waves vertically inside the SemiVO_2 film and holes or horizontally along the film's planar interfaces, thus diverting optical energy away from the zero-order transmission channels. These FP modes arise almost exclusively in the SemiVO_2 phase because its optical constants, unlike those of MetVO_2, are almost non-dispersive and mostly real-valued within a wide spectral range [Fig. 1(c–f)]. At vacuum wavelengths in the range λ = 600–1000 nm, SemiVO_2 acts as a slightly lossy dielectric with a nearly constant refractive index n_{semi} = 2.9–3.0 [Fig. 1(e), dashed-line box] and a relatively

OSA CONTINUUM

small extinction coefficient $\kappa_{semi} = 0.35–0.50$ [Fig. 1(f)]. As the hole diameter and VO_2 thickness are swept through values that fulfill FP (anti-)resonance conditions, in-plane and vertical modes in the perforated SemiVO_2 film "trap" some of the light emerging from the perforated Au (or Ag) film, thus diminishing the EOT through the bilayer hole array in the semiconducting state. Since the refractive index of MetVO_2 varies substantially ($n_{met} = 1.7–2.5$) and the extinction coefficient is larger ($\kappa_{met} = 0.46–1.4$) in this spectral range, FP-type light-trapping modes are suppressed and the holes in the VO_2 film "funnel" the transmitted light more effectively in the metallic state. In addition to FP (anti-)resonances with symmetric Lorentzian profiles, our perforated bilayers exhibit the usual Fano-profile spectral shapes expected of EOT peaks [2,4,66–68]. Curiously, Fano-like profiles also emerge in the dependence of the *M2S-ratios* on array period or peak wavelength [Fig. 4 and Fig. 10(a)]. Fano lineshapes are discussed in Section 3.3.

2. Experimental measurements

The VO_2 films were fabricated by a combination of pulsed laser deposition (PLD) and thermal post-annealing, as previously reported in Ref. [69]. Upon switching, stoichiometrically correct VO_2 films show typically a 95% relative change in transmission intensity at 1550 nm and a ~5 °C hysteresis [Fig. 1(a)]. The desired VO_2 thickness was confirmed by measuring the step height by profilometry. A 200-nm-thick Au layer was deposited on top of the VO_2 layer via RF sputtering. Subsequently, 100×100 μm^2 arrays of holes were milled through the bilayer using a single-column focused ion beam (FIB). Hole arrays with periodicities of 650/845 nm and Au-hole diameters of 230/220 nm, respectively, were milled with an ion-beam diameter of 60 nm.

The optical setup for measuring the zero-order transmission (T_{00}) is shown schematically in Fig. S1(f, inset) and Fig. 2(e, inset). A 10× objective lens simultaneously focused incident light onto the sample and reflected light onto the charge-coupled-device (CCD) sensor of an imaging camera. Incident polarized white light was sent towards the sample through a 90:10 beamsplitter. Transmitted light was collected with an output lens and sent through an optical fiber to a grating spectrometer. T_{00} was measured in the semiconducting and metallic states of the VO_2 layer by varying and holding the temperature of the sample with a heating stage. The transmission hysteresis of the plain VO_2 film shown in Fig. 1(a) was measured with a similar setup, except for replacing the spectrometer with an optical power detector and a 1550-nm bandpass filter.

Scanning electron microscope (SEM) images at different magnifications (10k× and 35k×) of the Au + VO_2 hole array with $P_{array} \approx 650$ nm are shown in Fig. S1(a). The spiral scanning method used in FIB milling causes the inner part of the hole to have a higher exposure than the outside resulting in a conical hole shape that narrows with depth, with the top Au surface having larger-diameter opening apertures than the top surface of the underlying VO_2 layer. Grain analysis on one of the higher-magnification SEM images gave an average opening-aperture diameter $D_{Au(-holes)} \approx 230$ nm in the Au layer [Fig. S1(b)] and $D_{VO2(-holes)} \approx 125$ nm in the VO_2 layer [Fig. S1(c)]. The average periodicity in the *xy*-plane (i.e., sample surface) was determined by a two-dimensional fast-Fourier transform (2D-FFT) [Fig. S1(d)]; the reciprocal-space line profiles in the *x*- and *y*-directions are extracted in Fig. S1(e).

The experimental [Fig. S1(f)] and FDTD-simulated [Fig. S1(g, h)] spectra show good agreement for the EOT peak position, even as Fig. S1(a) reveals variations in hole shapes and diameters. The peak wavelength is primarily determined by the Bragg coupling condition for exciting surface plasmon polaritons on a periodically decorated metal-dielectric interface, which depends only on the lattice constant and indices of refraction of the materials [3]. The linewidths of the experimental transmission curves are larger than the simulated ones because the incident beam in the experiments includes non-zero components of in-plane wavevectors around normal incidence. The measured spectra exhibit asymmetric Fano-like profiles as expected from the phenomenological theory of EOT [2,4,66–68] and the numerical simulations. On the other hand, Fig. S1 makes it clear that a mismatch between hole diameters in the Au vs.

OSA CONTINUUM

VO_2 layer causes a significant difference in the *modulation* of the transmission between the metallic and semiconducting states of VO_2. The simulated M2S-ratio is 8.74 at $\lambda_{peak} = 698$ nm for $D_{VO2} = D_{Au} = 230$ nm (not shown), almost an order of magnitude higher than 1.15 ($\lambda_{peak} = 697$ nm) for $D_{VO2} = 125$ nm $< D_{Au} = 230$ nm [Fig. S1(g)]. The experimentally measured T_{00} peaks [Fig. S1(f)] have a ratio of 1.75 ($\lambda_{peak} = 778$ nm), which lies between these two simulated cases. In fact, by allowing for a margin of error in choosing the threshold pixel intensity in the image analysis of VO_2 aperture sizes in Fig. S1(c), where the scaling is ~7 nm/pixel, we simulate an intermediate case of $D_{VO2} = 165$ nm that yields M2S-ratio = 1.74 ($\lambda_{peak} = 697$ nm) [Fig. S1(h)], almost equal to the experimental value. (See Supplement 1 for supporting content.)

A similar analysis of the larger-period Au + VO_2 hole array is presented in Fig. 2. The electron micrographs in Fig. 2(a) were taken at the same magnifications as those in Fig. S1(a). Grain [Fig. 2(b)] and 2D-FFT [Fig. 2(c, d)] analyses of the SEM images yield $D_{Au} \approx 220$ nm and $P_{array} \approx 845$ nm. Unlike Fig. S1(a), Fig. 2(a) does not reveal the underlying VO_2 layer, so we assume $D_{VO2} = D_{Au} \approx 220$ nm. It appears that the larger dose and nominally specified hole diameter (310 nm) resulted in more uniform milling through the Au and VO_2 layers. The experimental results [Fig. 2(e)] are in better agreement with both the FDTD [Fig. 2(f)] and FEM [Fig. 2(g)] simulations in terms of EOT switching: M2S-ratio = 2.21 ($\lambda_{peak} = 893$ nm) for the experimental, 2.60 ($\lambda_{peak} = 866$ nm) for the FDTD, and 2.58 ($\lambda_{peak} = 869$ nm) for the FEM spectra. Here too the larger linewidth and spectral shift of the measured peaks can be attributed to off-angle components

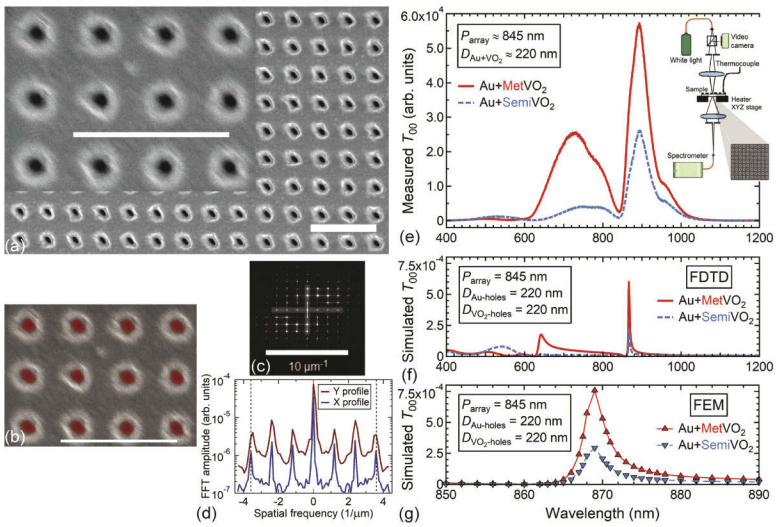

Fig. 2. Electron micrographs and measured vs. simulated zero-order transmission (T_{00}) spectra of another Au + VO_2 hole array milled through bilayer of 200-nm-thick gold film on top of 200-nm-thick VO_2 film on fused silica. **(a)** SEM images of portions of the array at lower and higher magnifications. **(b)** SEM image with masked (red) regions used to estimate average diameter of opening apertures: $D_{Au-holes} \approx D_{VO2-holes} \approx 220$ nm. **(c)** 2D-FFT image of lower-magnification micrograph in (a), with **(d)** horizontal (X) and vertical (Y) line profiles extracted to estimate array period: $P_{array} \approx 845$ nm in either direction. **(e)** Experimental T_{00} spectra through hole array in $MetVO_2$ and $SemiVO_2$ phases, measured with setup shown schematically in (e, inset). **(f)** FDTD and **(g)** FEM simulations of T_{00} spectra through hole array in each VO_2 phase. Scale bars: (a, b) 2 μm; (c) 10 μm^{-1}. Both measured and simulated T_{00} spectra for the 845-nm-period bilayer hole array exhibit *reverse switching*, i.e., higher peak transmission for $MetVO_2$ than $SemiVO_2$, in contrast to transmission through an unperforated VO_2 film [cf. Figure 1(b)].

OSA CONTINUUM

of in-plane wavevectors contained in the focal volume of the incident light. A secondary peak corresponding to a higher-order SPP mode is observed on the high-energy side of the main EOT peak.

Altogether, the experimental measurements on the two Air-Au + VO_2-Glass hole arrays of different periods reproduced well the reverse switching of EOT across the VO_2 phase transition. We also observed that the area fraction of the holes in the VO_2 layer affects the modulation ratio, an effect which we investigate computationally in Fig. 7.

3. Numerical simulations and Fano model

We used two different numerical methods [70], FDTD and FEM, in order to cross-check the computed results as well as exploit the advantages inherent in each technique. The FDTD and FEM results in this work are in good mutual agreement: within 2–3 nm for the peak positions and 5–15% differences in peak-transmission and switching-ratio values. For example, the FDTD spectra in the third panel of Fig. 3 ($P_{array} = 720$ nm) have peak-T_{00} values at $\lambda_{peak} = 757$ nm of 4.50×10^{-3} for $MetVO_2$ and 4.72×10^{-4} for $SemiVO_2$, resulting in M2S-ratio = 9.53; the corresponding FEM spectra (not shown) have peak-T_{00} values at $\lambda_{peak} = 759$ nm of 4.81×10^{-3} for $MetVO_2$ and 5.47×10^{-4} for $SemiVO_2$, and hence M2S-ratio = 8.79. Crucially, the overall EOT spectra as well as peak-T_{00} and M2S-ratio *trends* as a function of the various hole-array parameters are robustly consistent between the two simulation methods, warranting our treatment of the FDTD and FEM results as essentially interchangeable [e.g., cf. Figure 4(a, b)]. (See Supplement 1 for supporting content.)

3.1. Finite-difference time-domain (FDTD) method

The FDTD method [71,72] solves Maxwell's time-dependent curl equations directly on a discretized numerical grid. It approximates the derivatives of the electromagnetic field vectors as finite differences, sampled at discrete spatial and temporal points in a specific arrangement called a Yee cell [73]. We used the commercial software FDTD Solutions (v8.18.1262). The simulation domain spans an *xyz*-volume of $½P_{array} \times ½P_{array} \times 2200$ nm^3, where the overall ¼-factor stems from using the anti-symmetric condition (zero tangential electric field) at the *yz*-boundaries and the symmetric condition (zero normal electric field) condition at the *xz*-boundaries. Both *z*-boundaries are terminated with 128 stretched-coordinate perfectly matched layers (PML) to absorb the reflected and transmitted waves. The domain is discretized globally with a non-uniform conformal orthogonal mesh, which is overridden locally, within a volume that fully encloses all materials interfaces, with a finer uniform mesh of 2.5-nm increments. The incident illumination is an *x*-polarized plane wave, launched from the air side at normal incidence to the Au layer as a broadband pulse (400–1500 nm). Material dispersion curves [Fig. 1(c–f) for VO_2] are obtained within the software by fitting 'multi-coefficient models' to interpolated experimental data extracted from Verleur *et al.* [59] for VO_2 and Johnson and Christy [74] for Au/Ag. (See Supplement 1 for supporting content.)

3.2. Finite-element method (FEM)

Unlike the FDTD method, the FEM leaves Maxwell's equations intact but approximates the solution space by subdividing the computational domain into 'finite elements'—small geometric patches with locally defined polynomial approximations (interpolation functions) of the solution—and stitching the elements together under conditions of continuity of the tangential electric and magnetic fields [70]. The FEM results in this work were obtained with COMSOL Multiphysics (v4.4.0.150). The computational *xyz*-domain is $½P_{array} \times ½P_{array} \times \sim1500$ nm^3, with perfect electric conductor walls at the *yz*-boundaries and perfect magnetic conductor walls at the *xz*-boundaries. The air (vacuum) input medium, Au film, VO_2 film, glass substrate and hole subdomains are meshed adaptively with tetrahedral elements, which within the films and holes

OSA CONTINUUM

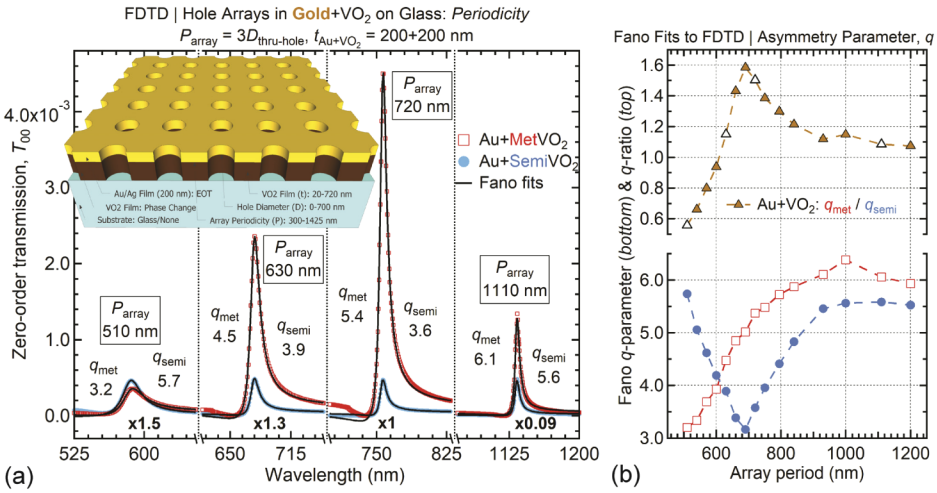

Fig. 3. Schematic of Au + VO_2 bilayer films on glass substrate (VO_2 layer in contact with glass), perforated by square periodic array of cylindrical holes. Incoming light illuminates Au-air interface as plane waves at normal incidence; transmitted light is detected in zero-order (normal) direction in substrate half-space. Ranges of geometrical parameters varied in simulations are written on the schematic: array period (P), hole diameter (D) and VO_2 film thickness (t). **(a)** FDTD spectra of zero-order transmission (T_{00}) for four P_{array} values, in $MetVO_2$ (open squares) and $SemiVO_2$ (solid circles) phases. Parameters: $t_{Au} = t_{VO2} = 200$ nm; $D_{thru-hole} \equiv D_{Au} = D_{VO2}$ scaled to $P_{array}/3$. Wavelength axis consists of four piecewise continuous segments separated by vertical dotted lines, with minor tick increments of 13 nm. Each pair of spectra are multiplied by factor shown underneath to scale $SemiVO_2$ peaks to same maximum value for better visualization of the non-monotonic SMPT-induced EOT modulation. Solid lines are analytical Fano-profile fits to spectra using Eq. (1), with corresponding q-parameter values listed for each pair of spectra. **(b)** Fano q-parameters extracted from Eq. (1) fits to FDTD T_{00} spectra for range of periods and hole diameters ($P_{array} = 3D_{thru-hole} = 510$–$1200$ nm): (bottom panel) q_{met} ($MetVO_2$, open squares) vs. q_{semi} ($SemiVO_2$, solid circles); (top panel) Met-to-Semi Fano q-ratio, q_{met}/q_{semi}; (top, open triangles) q-ratios for spectra shown in (a). The q-ratios follow a non-monotonic trend similar to that of the M2S-ratios in Fig. 4.

are set to grow no larger than 50 nm. Each z-boundary is capped with five sweep-meshed PMLs for absorbing the transmitted and reflected waves with minimal boundary reflections. Image plots of the electric-field intensity and power flow in different planes intersecting the unit cell are presented in Section 5. The Au and VO_2 optical constants used in the COMSOL simulations are extracted directly from the FDTD Solutions fits to ensure identical materials responses. (See Supplement 1 for supporting content.)

3.3. *Fano-profile fits*

Although a quantitative microscopic interpretation of EOT [9,11,12,15,75,76] began to emerge a full decade after the initial discovery, it had been recognized early on [66,67] that the dip-peak EOT spectra can be modeled very well [2,4,68,77–81] with a Fano-type formalism [82]. In the general Fano theory, a system's response function to an external perturbation acquires a characteristic *Fano profile* when a discrete resonant state interferes destructively (sharp dip) and constructively (asymmetric peak) with a continuum of states (or a broader spectral line) [83,84]. Specifically for EOT, discrete states can be any resonant surface electromagnetic modes (e.g., SPPs), while the continuum can include the (typically weak) direct transmission through the

OSA CONTINUUM

holes as well as any spectrally broad features (e.g., localized surface-plasmon resonances at the aperture rims [85]). A variation of the Fano-profile function for hole-array transmission [68,77] is given below, expressed in terms of the vacuum wavelength λ (in nm) rather than the customary frequency or energy:

$$T_{\mathrm{Fano}}(\lambda) = T_{\mathrm{b}} + T_{\mathrm{c}}\left(1 + q\frac{\frac{1}{2}\Lambda}{\lambda - \lambda_{\mathrm{res}}}\right)^2 \Bigg/ \left[1 + \left(\frac{\frac{1}{2}\Lambda}{\lambda - \lambda_{\mathrm{res}}}\right)^2\right] \tag{1}$$

The crucial *Fano parameter* q determines the asymmetry of the resonance. Being the cotangent of the phase shift between discrete and continuum modes, q is related to their coupling strength as well as to the relative excitation strengths—i.e., the ratio of resonant to non-resonant transmission amplitudes [66,79,84,86]. The term T_{b} is associated with the (background) portion of the direct transmission that is uncoupled from the discrete state, while T_{c} is associated with the zero-order continuum transmission that is coupled to and mixes with the discrete state. The resonance linewidth and position (both in nm) are given by Λ and λ_{res}, respectively. In general, the higher the $|q|$ value, the more symmetric, Lorentzian-like the lineshape becomes, signaling that the external perturbation (i.e., incident illumination) couples less efficiently to the continuum of scattering states. Conversely, as $q \to 0$, the external perturbation decouples from the discrete state and the Fano lineshape turns into an inverted-Lorentzian anti-resonance [84]. The most asymmetric lineshapes arise when $|q| = 1$.

The phenomenological Fano model does not reveal the microscopic origins of the different transmission channels (e.g., SPPs and quasi-cylindrical waves), but it does provide reasonably good fits to the EOT peaks, as Fig. 3(a) demonstrates. The solid lines are the best Fano fits [Eq. (1)] to the longest-wavelength EOT peaks simulated by FDTD for four representative Air-Au + VO_2-Glass hole arrays of different periods and thru-hole diameters ($D_{\mathrm{thru-hole}} \equiv D_{\mathrm{Au}} = D_{\mathrm{VO2}}$). (The spectra in this figure are scaled by the indicated factors to equalize the SemiVO_2 peak-T_{00} values for better visualization of the EOT modulation.) The extracted Fano asymmetry parameter q in Fig. 3(b, bottom panel) exhibits a different trend in each VO_2 phase with increasing P_{array} ($= 3D_{\mathrm{thru-hole}}$): q_{met} (open squares) grows almost monotonically from ~3 to ~6, whereas q_{semi} (solid circles) starts from ~6, dips through a minimum of ~3 at $P_{\mathrm{array}} = 690$ nm—close to 720 nm, where the highest M2S-ratio occurs [see Fig. 4(a)]—and then approaches ~6 at larger periods.

As mentioned above, the Fano q-parameter encodes the phase shift between the discrete (resonant) and continuum (direct, non-resonant) transmission channels [86,87]. Since q is related to the ratio of discrete-to-continuum excitation strengths, large resonant amplitudes and/or small continuum amplitudes should yield large $|q|$ values, and vice versa. The spectral position and intensity of the EOT peak depend on the lattice constant: λ_{peak} redshifts and peak-T_{00} increases with increasing P_{array}. The peak redshifts to satisfy momentum conservation and grows because good metals like Au and Ag allow SPPs to propagate with less dissipation at IR frequencies due to greater absorption lengths [88]. The resonant transmission channel (SPP modes) thus gets enhanced at larger array periods corresponding to longer resonant wavelengths (λ_{res}). The direct transmission channel, however, literally narrows at longer wavelengths as the skin depth of plasmonic metals decreases, which in turn shrinks the effective diameters of the holes [88]. Therefore, the combination of these effects tends to increase the Fano q-parameter as a function of periodicity, as reported in Ref. [68].

As seen in Fig. 3(b, bottom panel), q_{met} in the MetVO_2 state of the Air-Au + VO_2-Glass hole arrays also (mostly) increases with P_{array}, in line with the above reasoning. However, q_{semi} in the SemiVO_2 state varies non-monotonically with P_{array}, exhibiting a pronounced dip around $P_{\mathrm{array}} = 690$ nm ($\lambda_{\mathrm{peak}} = 730$ nm). Since the Fano q-parameter represents the ratio of resonant (SPPs) to continuum (direct evanescent transmission) contributions to T_{00}, the q_{semi} dip in Fig. 3(b, bottom panel) —and the corresponding $q_{\mathrm{met}}/q_{\mathrm{semi}}$ peak in Fig. 3(b, top panel)—could be caused by

OSA CONTINUUM

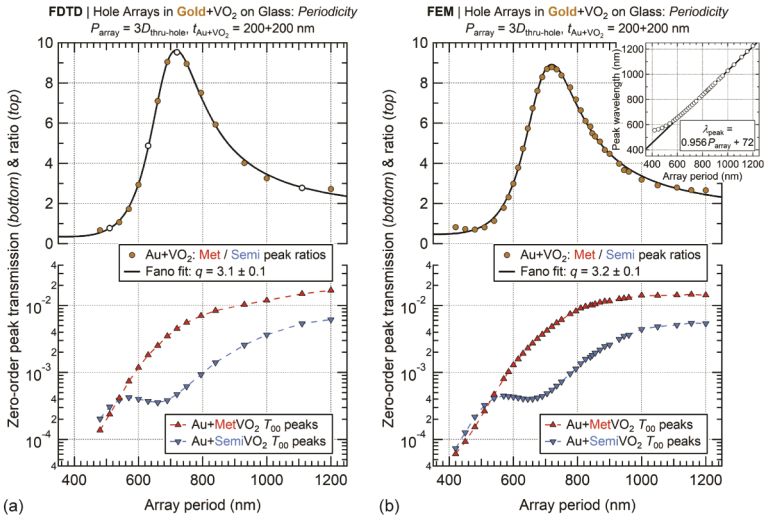

Fig. 4. **(a)** FDTD and **(b)** FEM simulations of zero-order transmission (T_{00}) as a function of array period ($P_{\text{array}} = 420$–1200 nm) through Au + VO_2 hole arrays on glass substrate. Thru-hole diameters are scaled as $D_{\text{thru-hole}} = P_{\text{array}}/3$; thickness of Au and VO_2 layers is fixed at 200 nm each for all periods. Areal aperture coverage is kept at $\pi(D_{\text{thru-hole}}/2)^2/(P_{\text{array}})^2 = \pi[(D_{\text{thru-hole}}/2)/(3D_{\text{thru-hole}})]^2 = \pi/36 = 8.7\%$. Bottom panels show peak-T_{00} values in the metallic phase ($MetVO_2$) and corresponding (i.e., at same wavelength) T_{00} values in the semiconducting phase ($SemiVO_2$) of the VO_2 layer. For each P_{array}, transmission values in both phases are taken at peak-T_{00} wavelength for $MetVO_2$ (λ_{peak}), which is redshifted from $\lambda_{\text{Rayleigh}} = P_{\text{array}}$ by 54 nm for $P_{\text{array}} = 600$ nm, 39 nm for $P_{\text{array}} = 720$ nm, 26 nm for $P_{\text{array}} = 1200$ nm, etc. Inset in (b, top) plots dependence of λ_{peak} on P_{array}; best linear fit within $P_{\text{array}} = 600$–1200 nm range yields $\lambda_{\text{peak}} = 0.956P_{\text{array}} + 72$ nm. Top panels show M2S-ratios of peak-T_{00} values from bottom panels. Open circles in (a, top) correspond to four pairs of spectra in Fig. 3(a); solid lines are analytical Fano-profile fits with equal Fano parameters ($q \approx 3$), using generalized form of Eq. (1). Both simulation methods produced well-converged, closely matching spectra, which justifies using FDTD and FEM results interchangeably. Maximum M2S-ratio = 10 at $P_{\text{array}} = 720$ nm and $\lambda_{\text{peak}} = 758$ nm.

one or more interactions that decrease q_{semi} at specific values of the structural parameters: weaker coupling of the external illumination to the resonant channel; stronger coupling of the external illumination to the continuum transmission channel; and/or a more effective coupling *between* this (SPPs) or another (e.g., FP modes) resonant channel and the reflection continuum [89]. In other words, when geometry (e.g., $P_{\text{array}} = 690$ nm, $D_{\text{thru-hole}} = 230$ nm, $t_{\text{Au}} = t_{\text{VO2}} = 200$ nm) and the VO_2 optical properties ($n_{\text{semi}} + i\kappa_{\text{semi}} \approx 3 + 0.4i$ for $\lambda = 600$–1000 nm) "conspire" to make the EOT lineshapes more Fano-like (i.e., more asymmetric) as $q_{\text{semi}} \rightarrow 3$, interference between the discrete and continuum channels reduces the zero-order transmission. The results in Section 4 seem to point to FP-type anti-resonances as the discrete modes that produce the recurring dips ("valleys") observed in the $SemiVO_2$ phase as a function of array period [Fig. 4 and Fig. 10(a)], VO_2 film thickness [Fig. S2(a) and Fig. 5(a)], thru-hole diameter [Fig. S2(b) and Fig. 6(a)], VO_2-hole diameter [Fig. 7(a)], VO_2 absorption [Fig. S3(a)] and $SemiVO_2$ refractive index (Fig. 9).

3.4. *Parameter space explored via FDTD and FEM simulations*

We have performed the following parameter sweeps (listed in Supplement 1) of hole-array geometry and VO_2 optical constants in order to optimize the Met-to-Semi EOT switching (i.e.,

OSA CONTINUUM

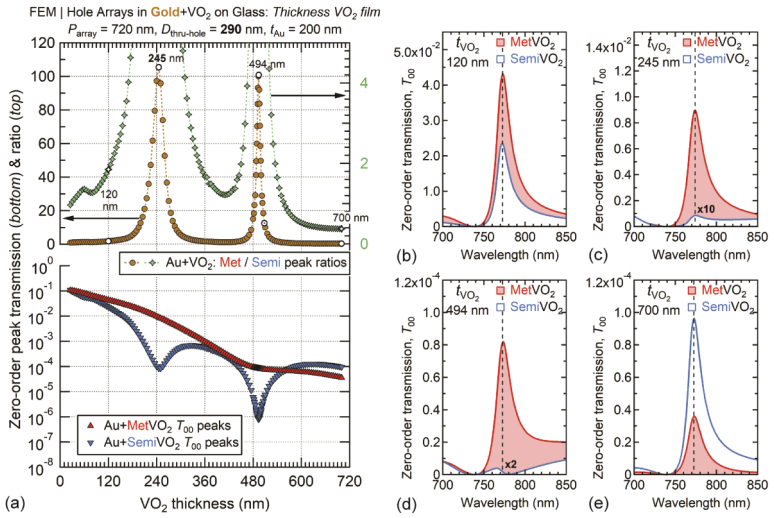

Fig. 5. FEM simulations of Au + VO_2 hole arrays on glass. **(a)** Varying thickness of VO_2 layer (t_{VO2} = 25–700 nm) at fixed period (720 nm), thru-hole diameter (290 nm) and Au-layer thickness (200 nm): (bottom panel) Peak-T_{00} values in $MetVO_2$ and $SemiVO_2$ phases, spanning λ_{peak} = 771–775 nm wavelength range, with vertical dashed lines in (b–e) marking specific λ_{peak} values; (top panel, left axis, circles) M2S-ratios on full scale; (top panel, right axis, diamonds) same M2S-ratios on magnified scale. T_{00} spectra for open markers in (a, top) at representative values of t_{VO2}: **(b)** 120 nm; **(c)** 245 nm ($SemiVO_2$ spectrum multiplied by 10); **(d)** 494 nm ($SemiVO_2$ spectrum multiplied by 2); and **(e)** 700 nm. Dotted circle in (a, top) marks t_{VO2} = 508 nm for comparison with Fig. S2(a, top): no deep M2S-ratio minimum here. Maximum M2S-ratio = 105 at t_{VO2} = 245 nm and λ_{peak} = 774 nm; second maximum M2S-ratio = 101 at t_{VO2} = 494 nm and λ_{peak} = 773 nm.

maximize the M2S-ratio) and intuit why T_{00} is generally higher in the $MetVO_2$ phase of the perforated bilayers. The "(Au)" or "(Ag)" designation after a Roman numeral means that the given optimization sweep applies to gold + VO_2 hole arrays on a glass substrate or freestanding silver + VO_2 hole arrays. The thickness of the Au and Ag layers in all simulations is kept constant at 200 nm.

The geometric iterations of Au + VO_2 hole arrays produced an optimized perforated bilayer with M2S-ratio = 196 [Fig. 7(a)] at λ_{peak} = 778 nm for P_{array} = 720 nm, D_{Au} = 302 nm, D_{VO2} = 304 nm, t_{Au} = 200 nm, t_{VO2} = 245 nm. A close second Au + VO_2 hole array with M2S-ratio = 188 [Fig. 6(a)] differs only in $D_{VO2} = D_{Au}$ = 302 nm. Since it would be difficult in practice to tune D_{VO2} with 2-nm precision, we take the latter (equal diameters) as the "gold standard" in terms of EOT modulation, which is shown in Fig. 6(c), Fig. 12(c, d) and Fig. 13(c, d, h). Although we explored the parameter space of perforated Au + VO_2 on glass in more detail than that of perforated freestanding Ag + VO_2, we simulated enough of the latter structures to observe the same trends in EOT modulation —for instance, compare Fig. 4(a) and Fig. 10(a). Therefore, the results shown below for Au + VO_2 hole arrays apply just as well to Ag + VO_2 hole arrays. (See Supplement 1 for supporting content.)

OSA CONTINUUM

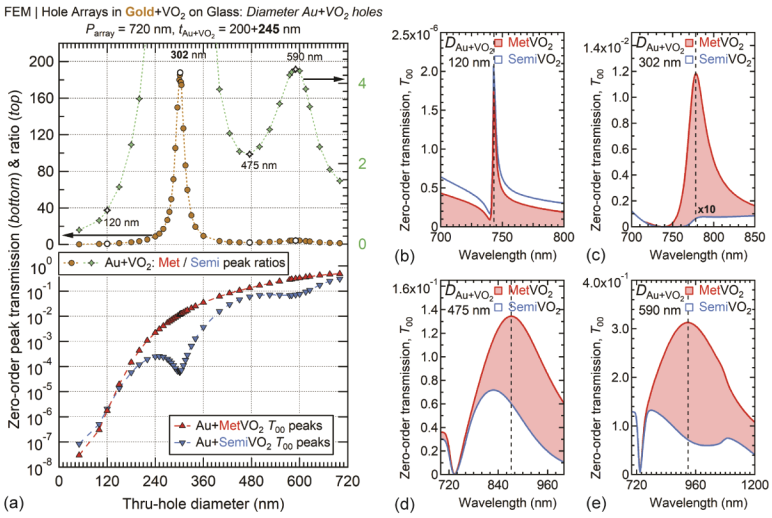

Fig. 6. FEM simulations of Au + VO_2 hole arrays on glass. **(a)** Varying thru-hole diameter ($D_{\text{thru-hole}} \equiv D_{\text{Au+VO2}}$ = 50–700 nm) at fixed period (720 nm), Au-layer thickness (200 nm) and VO_2-layer thickness (245 nm): (bottom panel) Peak-T_{00} values in $MetVO_2$ and $SemiVO_2$ phases, spanning λ_{peak} = 741–980 nm wavelength range, with vertical dashed lines in (b–e) marking specific λ_{peak} values; (top panel, left axis, circles) M2S-ratios on full scale; (top panel, right axis, diamonds) same M2S-ratios on magnified scale. T_{00} spectra for open markers in (a, top) at representative values of $D_{\text{thru-hole}}$: **(b)** 120 nm; **(c)** 302 nm ($SemiVO_2$ spectrum multiplied by 10) [see also Fig. 12(c, d) and Fig. 13(c, d, h)]; **(d)** 475 nm; and **(e)** 590 nm. Maximum M2S-ratio = 188 at $D_{\text{thru-hole}}$ = 302 nm and λ_{peak} = 778 nm; this is the "gold standard" Au + VO_2 hole array of this work.

OSA CONTINUUM

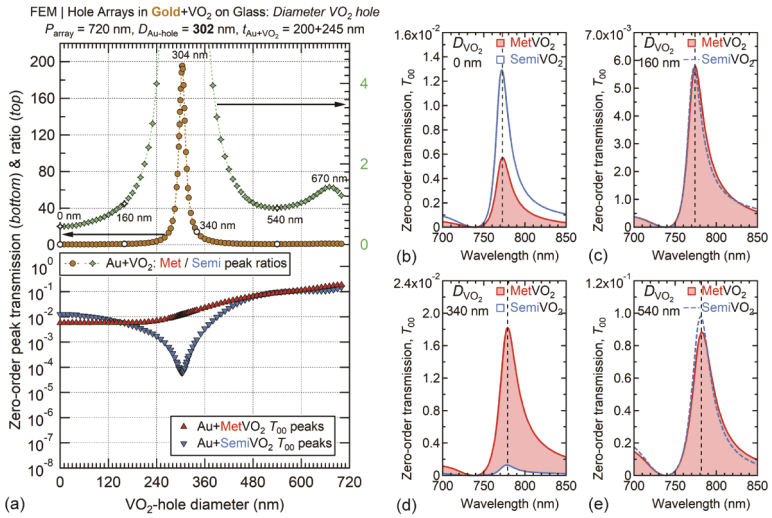

Fig. 7. FEM simulations of Au + VO_2 hole arrays on glass. **(a)** Varying hole diameter only in VO_2 layer (D_{VO2} = 0–700 nm) at fixed period (720 nm), Au-hole diameter (302 nm), Au-layer thickness (200 nm) and VO_2-layer thickness (245 nm): (bottom panel) Peak-T_{00} values in $MetVO_2$ and $SemiVO_2$ phases, spanning λ_{peak} = 773–787 nm wavelength range, with vertical dashed lines in (b–e) marking specific λ_{peak} values; (top panel, left axis, circles) M2S-ratios on full scale; (top panel, right axis, diamonds) same M2S-ratios on magnified scale. T_{00} spectra for open markers in (a, top) at representative values of D_{VO2}: **(b)** 0 nm [i.e., unperforated VO_2 layer; see also Fig. 12(a, b)]; **(c)** 160 nm [see also Fig. 13(a, b, g)]; **(d)** 340 nm; and **(e)** 540 nm [see also Fig. 13(e, f, i)]. Maximum M2S-ratio = 196 at D_{VO2} = 304 nm, D_{Au} = 302 nm and λ_{peak} = 778 nm.

OSA CONTINUUM

4. Simulation results: zero-order transmission peaks, ratios, and spectra

4.1. Varying array period for Air-Au + VO_2-Glass hole arrays

Optimization I(Au): max(M2S-ratio) ≈ 10 at $\lambda_{peak} = 758$ nm and $P_{array} = 720$ nm.

The periodic separation of the holes in the *xy*-plane, P_{array}, is the key parameter that determines the spectral location of the EOT peak, λ_{peak}, associated with the air-metal interface under normal-incidence illumination. Therefore, it is reasonable to start the optimization process of maximizing the EOT switching by varying P_{array} for typical values of film thickness ($t_{Au} = t_{VO2} = 200$ nm) and hole diameter ($D_{Au} = D_{VO2} = P_{array}/3$). The simulated peak-$T_{00}$ in each VO_2 phase and the corresponding M2S-ratios are shown in Fig. 4(a) for the FDTD and Fig. 4(b) for the FEM optimization runs.

To a first approximation, λ_{peak} is governed by the SPP dispersion relation for an unperforated metal-dielectric interface, augmented by integer multiples of the reciprocal lattice vectors of the periodic hole array in order to bridge the momentum mismatch between the freely propagating incident light and the bound SPP modes [3,90]. When the Fano-type interferences [66] described in Section 3.3 are considered, λ_{peak} is always redshifted by some tens of nanometers with respect to P_{array}, as Fig. 3(a) demonstrates visually and the inset in Fig. 4(b, top panel) quantifies via a linear fit. Intriguingly, not only do T_{00} spectra exhibit Fano lineshapes [e.g., see Fig. 3(a)], but peak-T_{00} *ratios* vs. P_{array} (or vs. λ_{peak}) also follow closely the Fano-profile function [solid lines in Fig. 4 and Fig. 10(a), top panels], in a generalized form of Eq. (1). Since peak-T_{00} for MetVO_2 increases monotonically with array period, the Fano-like shapes of these M2S-ratio curves stem from the SemiVO_2 peak-T_{00} "valley" in the 550–700 nm spectral region [Fig. 4 and Fig. 10(a), bottom panels], which overlaps the largely non-dispersive region of $n_{semi}(\lambda = 600\text{–}1000\,\text{nm})$ mentioned in Section 1 and highlighted in Fig. 1(e).

4.2. Varying VO_2 thickness and thru-hole diameter for Air-Au + VO_2-Glass hole arrays

Optimizations II(Au) & III(Au): max(M2S-ratio) = 12 at $\lambda_{peak} = 759$ nm and $t_{VO2} = 220$ nm; max(M2S-ratio) = 36 at $\lambda_{peak} = 774$ nm and $D_{thru-hole} = 290$ nm. (See Supplement 1 for supporting content.)

After determining the optimal array period, we fix P_{array} (720 nm), $D_{thru-hole}$ (240 nm = 720 nm/3) and t_{Au} (200 nm), and then sweep the thickness of the VO_2 layer, t_{VO2}. Peak-T_{00} values decrease in both phases as the VO_2 layer gets thicker [Fig. S2(a)], as expected from Beer's law for light traversing a lossy dielectric film. (The air-filled holes do not contribute to the dissipative absorption.) The FEM results reveal pronounced dips in SemiVO_2 peak-T_{00} that bring about a primary peak and a smaller secondary peak in the M2S-ratio at $t_{VO2} = 220$ nm and $t_{VO2} = 570$ nm, respectively. It is not obvious if these t_{VO2} values fulfill specific FP conditions.

A puzzling feature is the very sharp dip in the *Met*VO_2 state at $t_{VO2} = 510$ nm—unique because the simulated MetVO_2 peak-T_{00} curves in all the other Au + MetVO_2 hole arrays behave monotonically as a function of the geometrical parameters. To better visualize this dip, the top panel of Fig. S2(a) plots the *inverse* 1/M2S-ratio (diamond markers, right-axis scale): Note that this steep, inverted ($q_{1/M2S} < 0$) Fano profile reaches a maximum at $t_{VO2} = 508$ nm, where the Fano profile of the secondary M2S-ratio peak ($q_{M2S} > 0$) has its minimum.

The next step is to sweep $D_{thru-hole}$ at fixed P_{array} (720 nm), t_{Au} (200 nm) and the just-optimized t_{VO2} (220 nm). The FEM results are shown in Fig. S2(b). As expected [6,7,79,91], the transmission is very weak for deeply subwavelength holes—e.g., $T_{00} < 10^{-7}$ at $\lambda = 740$ nm for $D_{thru-hole} = 50$ nm—but grows rapidly as the aperture is widened towards the (material-dependent) cutoff diameter for propagating guided modes, and then saturates thereafter. The transmission peaks also broaden [cf. Figure 6(b–e)] and redshift with increasing diameter, caused by, respectively, increased radiative damping and the nonlinear dependence of transmission on wavelength below cutoff [4,79,91]. The inset in Fig. S2(b) empirically quantifies the

OSA CONTINUUM

redshift of the peak position via a quadratic fit. The M2S-ratio as a function of $D_{\text{thru-hole}}$ [Fig. S2(b), top panel] exhibits a primary peak at $D_{\text{thru-hole}} = 290$ nm and a smaller secondary peak at $D_{\text{thru-hole}} = 580\,\text{nm} = 2 \times 290\,\text{nm}$. The Lorentzian lineshapes and integer scaling strongly suggest that these two peaks arise from consecutive standing-wave modes of a Fabry-Perot (anti-)resonance.

4.3. Varying VO_2 thickness (2nd iteration) for Air-Au + VO_2-Glass hole array

Optimization IV(Au): max(M2S-ratio) = 105 at $\lambda_{\text{peak}} = 774$ nm and $t_{\text{VO2}} = 245$ nm.

The iterative process of maximizing the EOT switching continues by varying the thickness of the VO_2 layer, t_{VO2}, once again at fixed P_{array} (720 nm), t_{Au} (200 nm) and $D_{\text{thru-hole}}$, but this time with the latter having the newly found optimal value of 290 nm. The FEM results for the peak-T_{00} and M2S-ratio are shown in Fig. 5(a), while Fig. 5(b–e) display the pairs of simulated T_{00} spectra, in each VO_2 phase, for the four representative open-circle markers in Fig. 5(a, top panel). The MetVO_2 peak-T_{00} curve in Fig. 5(a, bottom panel) also trends downwards with increasing t_{VO2}, as it does in Fig. S2(a), but instead of a pronounced dip around $t_{\text{VO2}} = 510$ nm, this curve gently plateaus. The SemiVO_2 peak-T_{00} trend resembles that in Fig. S2(a), but with notable differences: the two dips in Fig. 5(a) are much sharper and the second one is located at almost exactly double the t_{VO2} value of the first one: 494 nm vs. 245 nm. Owing to the greater depth of these SemiVO_2 peak-T_{00} minima, the two prominent M2S-ratio peaks in Fig. 5(a, top panel) exceed 100 [cf. Fig. S2(a, top panel)].

The two t_{VO2} values, 245 nm and 494 nm $\approx 2 \times 245$ nm, for which the M2S-ratio maxima and corresponding SemiVO_2 peak-T_{00} minima occur in Fig. 5(a), suggest the involvement of (anti-)resonant FP modes spaced in t_{VO2} by an integer number of half wavelengths $\lambda_{\text{semi}}/2$ inside the SemiVO_2 material, where $\lambda_{\text{semi}} = \lambda_{\text{vac, peak}}/n_{\text{semi}}(\lambda_{\text{vac, peak}}) = 773\,\text{nm}/2.89 = 267$ nm ~ 245 nm. As to why these presumably consecutive modes are spaced by nearly two half wavelengths rather than one, we speculate that non-zero phase changes on reflection at the materials interfaces also contribute to the FP resonance conditions [64,65], in addition to the accumulated optical-path-length phase due to the waves traversing the thickness of the VO_2 layer.

The SemiVO_2 T_{00} spectrum in Fig. 5(d), which is largely responsible for the narrow M2S-ratio peak at $t_{\text{VO2}} = 494$ nm in Fig. 5(a, top panel), has a distinctly different shape from the other spectra in this set. Upon comparing Fig. 5(d) with Fig. 5(b, c, e), it appears that the SemiVO_2 spectrum for $t_{\text{VO2}} = 494$ nm should have had a peak around $\lambda_{\text{peak}} = 773$ nm, more or less aligned with the peak of the corresponding MetVO_2 spectrum, but instead has a small blueshifted peak ($\lambda = 737$–780 nm) and a very broad redshifted "hill" ($\lambda > 780$ nm), with a deep valley in between ($T_{00} < 10^{-7}$ at $\lambda = 780$ nm). Curiously, this SemiVO_2 spectrum resembles the MetVO_2 spectrum (not shown) associated with the feature at $t_{\text{VO2}} = 510$ nm in Fig. S2(a, bottom panel) (see Section 4.2). Such an abrupt change from a peak to a dip at $t_{\text{VO2}} = 494$ nm is further evidence of an FP-type anti-resonance of waves undergoing destructive interference in the z-direction in the VO_2 film *and* within the holes that perforate it, after reflections at the Au-VO_2 and VO_2-glass xy-interfaces. Additional FEM simulations (not shown) confirm that the holes in the VO_2 layer are crucial for the resonant mechanism, since varying t_{VO2} as in Fig. 5 but *without perforating the VO_2 layer* generates an approximately exponential decay of the M2S-ratio that never exceeds 1.45 for any VO_2 thickness in this range.

4.4. Varying thru-hole diameter (2nd iteration) for Air-Au + VO_2-Glass hole arrays

Optimization V(Au): max(M2S-ratio) = 188 at $\lambda_{\text{peak}} = 778$ nm and $D_{\text{thru-hole}} = 302$ nm.

An additional increase in the Met-to-Semi switching ratio is achieved by a second tuning of the diameter $D_{\text{thru-hole}}$ (also labeled $D_{\text{Au+VO2}}$) of the thru-holes (Fig. 6), after setting the VO_2 thickness to the optimal t_{VO2} value (245 nm) from Fig. 5(a). The new optimal value $D_{\text{thru-hole}} = 302$ is somewhat larger than the one found in Fig. S2(b), 290 nm, and the dips in the SemiVO_2 peak-T_{00}

OSA CONTINUUM

curve are sharper, indicating that the vertical (z-direction) FP resonances as a function of VO_2 thickness are coupled in some way with the lateral (xy-plane) FP resonances as a function of hole diameter [63]. In other words, different t_{VO2} values lead to a different position, width and depth of the primary M2S-ratio peak that emerges during a $D_{thru-hole}$ sweep [cf. Fig. S2(b) and Fig. 6(a), top panels]. As already mentioned in Section 4.2 and demonstrated in Fig. 6(b–e), T_{00} spectral peaks broaden and redshift with increasing $D_{thru-hole}$. In the semiconducting state, the T_{00} spectra also change shape at values of $D_{thru-hole}$ where the M2S-ratio has primary and secondary maxima: 302 nm [Fig. 6(c)] and 590 nm $\approx 2 \times 302$ nm [Fig. 6(e)]. The near-integer scaling points again to lateral FP-type anti-resonances in the SemiVO_2 transmission.

4.5. Varying hole diameter only in VO_2 layer for Air-Au + VO_2-Glass hole arrays

Optimization VI(Au): max(M2S-ratio) = 196 at $\lambda_{peak} = 778$ nm and $D_{VO2} = 304$ nm.

It was already demonstrated in Fig. S1(g, h) that D_{VO2}, the diameter of holes in the VO_2 layer alone, affects the M2S-ratio. When $D_{VO2} << D_{Au}$, the VO_2 layer optically resembles an unperforated film in that most of the light emerging from the holes in the Au layer traverses VO_2 material rather than air-filled waveguides embedded in it, and transmission in the semiconducting state exceeds that in the metallic state. In Fig. 7(a), FEM simulations of T_{00} through hole arrays with a fixed Au-hole diameter ($D_{Au} = 302$ nm) and variable VO_2-hole diameter show M2S-ratio < 1 for $D_{VO2} \leq 150$ nm. In the limit of vanishing holes in the VO_2 layer, the Fresnel-calculated transmission ratio at $\lambda = 773$ nm for a plain VO_2 film on glass (i.e., no Au layer) in Fig. 1(b) and the M2S-ratio for a half-perforated bilayer on glass (i.e., holes only in the Au layer) in Fig. 7(b) are quite similar: $T_{PlainMetVO2}/T_{PlainSemiVO2} = 0.39$ vs. M2S-ratio($D_{VO2} = 0$ nm) = 0.45. Conversely, as D_{VO2} is increased beyond D_{Au}, less and less of the light emerging from the Au holes interacts with VO_2 material and thus the EOT modulation diminishes: for $D_{VO2} > 480$ nm, M2S-ratio = 1.0–1.4.

Between the two regimes, the switching ratio rises to 196 at $D_{VO2} = 304$ nm as the SemiVO_2 peak-T_{00} drops two orders of magnitude. This (anti-)resonant D_{VO2} hole diameter is only 2 nm larger than the fixed $D_{Au} = 302$ nm hole diameter and M2S-ratio = 196 is only marginally higher than the "gold standard" M2S-ratio = 188 optimized in Section 4.4 by varying the $D_{thru-hole}$ diameter of holes in both layers. However, there is a difference of several orders of magnitude in how peak-T_{00} scales with varying $D_{thru-hole}$ vs. varying only D_{VO2}. For the thru-hole diameter sweep, the maximum transmission spans $\sim 10^{-8}$–1 [Fig. 6(a), bottom panel], while for the VO_2-hole diameter sweep the $\sim 10^{-4}$–10^{-1} range is much smaller [Fig. 7(a), bottom panel]. The widths, spectral positions and shapes of the T_{00} peaks also differ between the two sweeps. Peaks broaden and redshift significantly with increasing $D_{thru-hole}$, and even begin to split for SemiVO_2 [e.g., see Fig. 6(e)], whereas they remain qualitatively unchanged with increasing D_{VO2}, as seen in the T_{00} spectra in Fig. 7(b–e).

4.6. Varying (hypothetically) VO_2 absorption for Air-Au + VO_2-Glass hole array

Optimization VII(Au): max(M2S-ratio) = 220 at $\lambda_{peak} = 778$ nm and $\varepsilon_{imag} \times 1.05$. (See Supplement 1 for supporting content.)

The parameter sweep presented in Fig. S3 is "hypothetical" since the VO_2 permittivity cannot be easily tuned experimentally; besides, the imaginary part $\varepsilon_{imag} \equiv \mathrm{Im}[\varepsilon_{VO2}(\lambda)]$ cannot be varied independently of the real part as the two parts of the dielectric response function are linked via causality-imposed Kramers-Kronig (K-K) relations [92]. Nevertheless, it is informative to simulate EOT spectra through perforated bilayers consisting of a regular Au film and a hypothetical "VO_2" film with artificially modified absorption, i.e., $\alpha\ \varepsilon_{imag}$, where α is a real-valued positive scaling factor. By leaving the real part of the VO_2 permittivity unchanged, we manually override the K-K relations in this set of FEM simulations. As Fig. S3(a) demonstrates, when the ε_{imag} functions of both SemiVO_2 and MetVO_2 are multiplied by a factor α substantially lower or

OSA CONTINUUM

higher than unity, the M2S-ratio drops steeply from its maximum value of 220 at $\alpha = 1.05$ [Fig. S3(d)] down to about 20 at $\alpha = 0.10$ [Fig. S3(b)] and $\alpha = 0.50$ [Fig. S3(b)] or about 2 at $\alpha = 3.00$ [Fig. S3(e)]. The M2S-ratio peak around $\alpha \approx 1$ once again appears to be caused by an FP-type anti-resonance in the $SemiVO_2$ transmission, whereas the $MetVO_2$ transmission decreases slowly and monotonically with increasing artificial absorption (i.e., α). For low absorption ($\alpha << 1$), both $MetVO_2$ and $SemiVO_2$ become nearly lossless dielectrics, and there is not a pronounced dip in the $SemiVO_2$ peak-T_{00}, probably because the lower values of $\alpha\ \varepsilon_{imag}$ modify the reflected waves' phase changes on reflection [64] at the Au-$SemiVO_2$ and $SemiVO_2$-glass interfaces in ways that render the FP anti-resonance condition unfulfilled. In the high-absorption limit ($\alpha >> 1$), the electromagnetic fields are strongly attenuated as the waves traverse either $MetVO_2$ or $SemiVO_2$, the differential interfacial reflections diminish, and hence the M2S-ratio approaches unity (e.g., M2S-ratio = 1.62 for $\alpha = 4$).

4.7. Varying (hypothetically) refractive index of material inside holes in VO_2 layer

Optimization VIII(Au): max(M2S-ratio) = 188 at $\lambda_{peak} = 778$ nm and $n_{HoleVO2} = 1.00$.

The parameter sweep in Fig. 8 is also hypothetical because filling *only* the holes perforating the VO_2 layer with different dielectrics (e.g., index-matching fluids) would be experimentally unfeasible. While filling the Au + VO_2 thru-holes may be feasible, it would redshift the subwavelength regime of the holes by a factor equal to the refractive index of the filling material and thus unnecessarily complicate the interpretation of the EOT switching. Filling only the VO_2-layer holes keeps λ_{peak} nearly constant, as the four representative pairs of FEM-simulated (hypothetical) T_{00} spectra in Fig. 8(b–e) demonstrate. Simulating different refractive indices $n_{HoleVO2}$ of the material filling the VO_2-layer holes illustrates the idea that the VO_2 holes act as "light funnels" for the EOT emerging from the plasmonic hole array. As shown in Fig. 8(a, bottom panel), increasing $n_{HoleVO2}$ enhances peak-T_{00} for both $SemiVO_2$ and $MetVO_2$, but it does so more effectively in the semiconducting state because the waves tend to penetrate deeper into the plane of the perforated $SemiVO_2$ film, as opposed to the perforated $MetVO_2$ film where the light is more concentrated inside the holes.

Filling in the VO_2 holes with a dielectric of $n_{HoleVO2} > 1$ results in an exponential decrease—with two rate constants—of the M2S-ratio towards unity [Fig. 8(a, top panel)]. An exponential dependence can be understood from the fact that the peak wavelength inside the VO_2 holes is reduced to $\lambda_{peak}/n_{HoleVO2}$, which roughly equates to enlarging the hole diameter by the same factor. This increase in the effective D_{VO2} in turn leads to the tails of the evanescent waves, which are exponentially weaker away from the hole centers, to penetrate the cylindrical sidewalls with diminished amplitudes. Why the empirical fit works better with two rate constants instead of one is not entirely clear at this point, though it seems reasonable that this dependence may stem from the different trends of $SemiVO_2$ peak-T_{00} for $1 < n_{HoleVO2} < 1.6$ vs. $1.6 < n_{HoleVO2} < 3$ [Fig. 8(a, bottom panel)]. In terms of the maximum M2S-ratio($n_{HoleVO2} = 1.00$) = 188, this optimization affirms the "gold standard" of Optimization V(Au).

4.8. Varying (hypothetically) complex refractive index of semiconducting VO_2

Optimization IX(Au): max(M2S-ratio) = 3766 at $\lambda_{peak} = 787$ nm and $(n_{semi} + i\kappa_{semi}) \times 1.20$.

Another hypothetical parameter sweep is shown in Fig. 9(a, b). We start with the results from Fig. 4(b) for Air-Au + VO_2-Glass hole arrays with different periods (P_{array}) and corresponding thru-hole diameters ($D_{thru-hole} = P_{array}/3$), plotted as a function of peak wavelength (λ_{peak}) [see inset in Fig. 4(b) for P_{array}-to-λ_{peak} conversion]. We then perform a series of FEM simulations with the same geometries but with the refractive index, $n_{SemiVO2}(\lambda)$ [Fig. 9(c)], and extinction coefficient, $\kappa_{SemiVO2}(\lambda)$ [Fig. 9(d)], of semiconducting VO_2 scaled by an artificial multiplier, β—also manually overriding the K-K relations for this set of FEM simulations. The components of the complex refractive index of $MetVO_2$, also displayed in Fig. 9(c, d), are not modified. When

OSA CONTINUUM

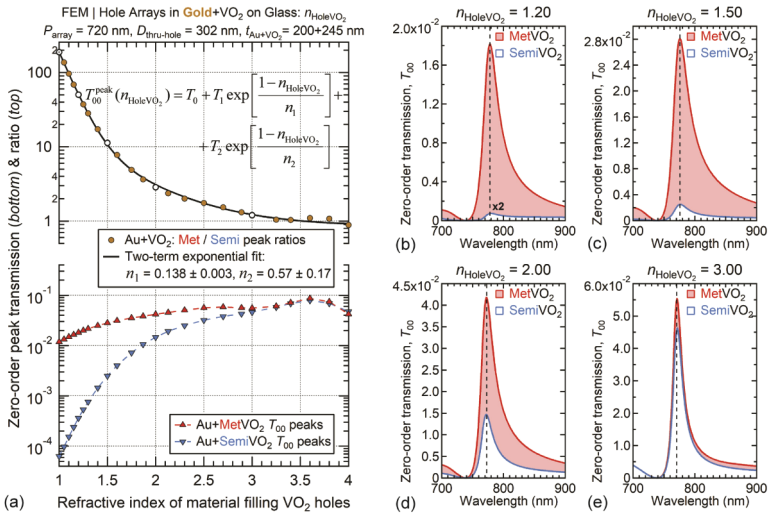

Fig. 8. FEM simulations of Au + VO_2 hole arrays on glass. **(a)** Hypothetically varying refractive index of material filling holes in VO_2 layer ($n_{HoleVO2}$ = 1.00–4.00) at fixed period (720 nm), thru-hole diameter (302 nm), Au-layer thickness (200 nm) and VO_2-layer thickness (245 nm): (bottom panel) Peak-T_{00} values in $MetVO_2$ and $SemiVO_2$ phases, spanning λ_{peak} = 770–778 nm wavelength range, with vertical dashed lines in (b–e) marking specific λ_{peak} values; (top panel, circles) M2S-ratios and (line) empirical fit using two-term exponential-decay function shown in inset, with best-fit parameters $T_0 = 0.86$, $T_1 = 176$, $n_1 = 0.14$, $T_2 = 12$ and $n_2 = 0.57$. T_{00} spectra for open circles in (a, top) at representative values of $n_{HoleVO2}$: **(b)** 1.20 ($SemiVO_2$ spectrum multiplied by 2); **(c)** 1.50; **(d)** 2.00; and **(e)** 3.00. Maximum M2S-ratio = 188 when VO_2 holes are filled with air (vacuum) [dotted circle in (a, top); see also Fig. 6(c)].

$\beta < 1$, the $SemiVO_2$ transmission curve as a function of λ_{peak} (or P_{array}) gradually loses the pronounced dip at λ_{peak} = 758 nm (or P_{array} = 720 nm), which occurs for $\beta = 1$, and rises above the $MetVO_2$ peak-T_{00} curve [Fig. 9(a, bottom panel)]. The corresponding M2S-ratios decrease from about 10 to less than 1 [Fig. 9(a, top panel)]. Conversely, when $\beta > 1$, the $SemiVO_2$ dip first deepens and sharpens substantially, before rising and flattening out again for $\beta > 1.20$ [Fig. 9(b, bottom panel)]. The dips also shift to longer peak wavelengths and larger array periods. At $\beta = 1.20$, the maximum M2S-ratio = 3766 at λ_{peak} = 787 nm and P_{array} = 750 nm [Fig. 9(b, top panel)].

The strong non-monotonic dependence of the $SemiVO_2$ dip and M2S-ratios on the $SemiVO_2$ refractive index provides further evidence that a Fabry-Perot (anti-)resonance is involved in the SMPT-induced EOT switching. In short, when the right geometrical and (hypothetical) material parameters combine in the perforated $SemiVO_2$ layer, transmission emerging from the adjacent plasmonic-layer hole array is attenuated as optical energy is channeled into FP-type modes.

4.9. Varying array period for Air-Ag+/–VO_2-Air hole arrays: with vs. without VO_2 holes

Optimization I(Ag): max(M2S-ratio) = 12 at λ_{peak} = 720 nm and P_{array} = 690 nm.

This section demonstrates that the SMPT-induced EOT switching mechanism is robust with respect to changing the plasmonic metal that generates the EOT effect, as well as dispensing with the glass substrate. The FDTD simulation results in Fig. 10(a) for freestanding silver + VO_2 hole arrays are very similar to those for gold + VO_2 arrays on glass in Fig. 4: (i) both M2S-ratio curves are fitted quite well to Fano profiles with $q \approx 3$ and linewidths of 170 nm (Ag + VO_2) and 200 nm (Au + VO_2); (ii) the maximum M2S-ratios are almost equal (12 vs. 10) and occur

OSA CONTINUUM

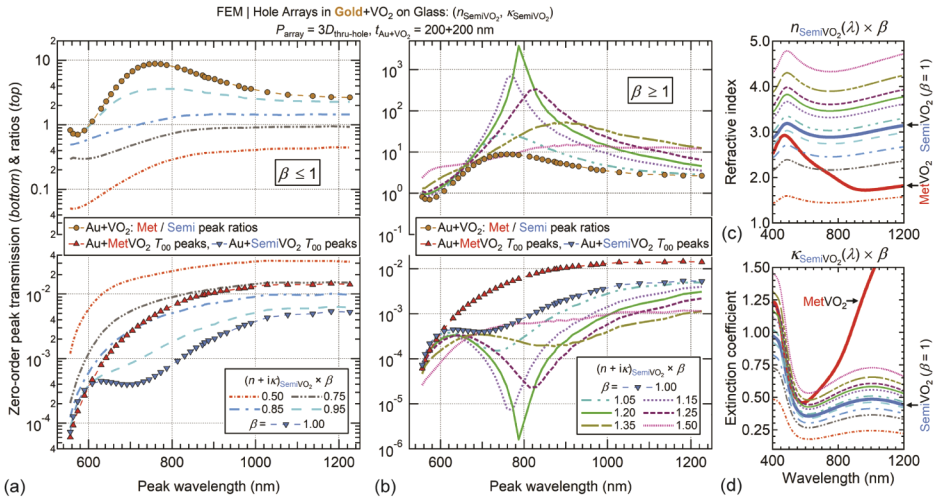

Fig. 9. FEM simulations of Au + VO_2 hole arrays on glass. Hypothetically varying refractive index ($n_{SemiVO2}$) and extinction coefficient ($\kappa_{SemiVO2}$) of semiconducting VO_2 via artificial multiplier ($\beta = 0.50$–1.50) for different array periods ($P_{array} = 420$–1200 nm) and thru-hole diameters ($D_{thru-hole} = P_{array}/3 = 140$–$400$ nm), at fixed Au-layer thickness (200 nm) and VO_2-layer thickness (200 nm). **(a)** (bottom panel, triangles) Peak-T_{00} values in the actual $MetVO_2$ and $SemiVO_2$ phases ($\beta = 1$), spanning $\lambda_{peak} = 556$–1226 nm wavelength range; (bottom panel, lines) hypothetical $SemiVO_2$ T_{00} values for $\beta < 1$, obtained at same λ_{peak} (and P_{array}) values as for $\beta = 1$; (top panel, circles) actual M2S-ratios; (top panel, lines) hypothetical M2S-ratios for $\beta < 1$. **(b)** Same as in (a) but for $\beta \geq 1$. **(c)** (thick lines) Actual $n_{MetVO2}(\lambda)$ and $n_{SemiVO2}(\lambda)$ dispersion curves [identical to Fig. 1(e)], and (thin lines) hypothetically scaled $n_{SemiVO2}(\lambda) \times \beta$ curves. **(d)** (thick lines) Actual $\kappa_{MetVO2}(\lambda)$ and $\kappa_{SemiVO2}(\lambda)$ dispersion curves [same as in Fig. 1(f)], and (thin lines) hypothetically scaled $\kappa_{SemiVO2}(\lambda) \times \beta$ curves. For a 120% hypothetical scaling ($\beta = 1.20$) of $n_{SemiVO2}(\lambda)$ and $\kappa_{SemiVO2}(\lambda)$, maximum M2S-ratio = 3766 at $P_{array} = 750$ nm and $\lambda_{peak} = 787$ nm, compared with 9 [see Fig. 4(b, top panel)] at $P_{array} = 720$ nm and $\lambda_{peak} = 758$ nm for the actual optical constants.

in the same 600–800 nm spectral window; (iii) both $SemiVO_2$ peak-T_{00} curves have "valleys" around 550–700 nm, while the $MetVO_2$ curves rise monotonically with increasing array period; and (iv) peak wavelengths in both cases scale linearly with array period. A minor difference is that the maximum M2S-ratio occurs at $P_{array} = 690$ nm ($\lambda_{peak} = 720$ nm) for Ag + VO_2 but at $P_{array} = 720$ nm ($\lambda_{peak} = 758$ nm) for Au + VO_2, although, for the former at $P_{array} = 720$ nm ($\lambda_{peak} = 749$ nm), M2S-ratio = 11 is hardly different from the maximum value.

Since the real part of the Ag permittivity is more negative than that of Au throughout the visible and infrared region (e.g., $\varepsilon_{Ag,\,real} = -29$ and $\varepsilon_{Au,\,real} = -22$ at 778 nm), for the same array period the Ag EOT peak is *less* redshifted than the Au EOT peak with respect to $\lambda_{Rayleigh} = P_{array}$, the so-called Rayleigh wavelength where the air-side (1,0) diffraction mode changes from radiative to evanescent (i.e., grazing to the surface). If we take the "gold standard" Air-Au + VO_2-Glass hole array—with maximum M2S-ratio ≈ 190 at $\lambda_{peak} = 778$ nm, $P_{array} = 720$ nm, $D_{thru-hole} = 302$ nm and $t_{VO2} = 245$ nm [Section 4.4 and Fig. 6(c)]—and only swap the gold layer for a silver layer, then the simulated Air-Ag + VO_2-Glass EOT peaks (not shown) are closer to $\lambda_{Rayleigh}$, the Ag + $MetVO_2$ and Ag + $SemiVO_2$ peak-T_{00} values are, respectively, higher and lower than their Au + VO_2 counterparts, and the Ag + VO_2 M2S-ratio = 511 at $\lambda_{peak} = 767$ nm, although the overall T_{00} spectra for the two perforated bilayers are qualitatively the same. Perhaps coincidentally, at $\lambda = 778$ nm, the M2S-ratio for the Ag + VO_2 T_{00} spectra is also 190. The main takeaway is

OSA CONTINUUM

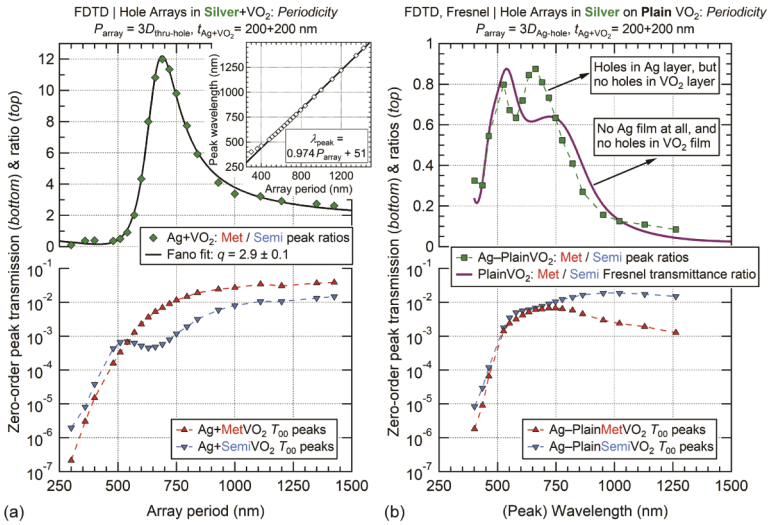

Fig. 10. FDTD simulations of hole arrays involving freestanding (no substrate) silver (Ag) and VO_2 bilayers in air, with fixed Ag-layer thickness (200 nm) and VO_2-layer thickness (200 nm). **(a)** Varying array period (P_{array} = 300–1425 nm) and thru-hole diameter ($D_{thru-hole} = P_{array}/3$ = 100–475 nm; 8.7% aperture coverage) of Ag + VO_2 hole arrays that perforate *both* layers: (bottom panel) Peak-T_{00} values in MetVO_2 and SemiVO_2 phases, spanning λ_{peak} = 402–1443 nm wavelength range; (top panel, solid diamonds) M2S-ratios and (line) Fano-profile fit with Fano parameter $q \approx 3$ (cf. Fig. 4), using generalized form of Eq. (1). Inset in (a, top) plots dependence of λ_{peak} on P_{array}; best linear fit within P_{array} = 480–1425 nm range yields $\lambda_{peak} = 0.974P_{array} + 51$ nm. **(b)** Varying array period (P_{array} = 300–1245 nm) and Ag-hole diameter ($D_{Ag} = P_{array}/3$ = 100–415 nm) of Ag–PlainVO_2 hole arrays that perforate only Ag layer while VO_2 layer remains intact: (bottom panel) Peak-T_{00} values in MetVO_2 and SemiVO_2 phases; (top panel, squares) M2S-ratios for Ag–PlainVO_2 hole arrays; (top panel, solid line) analytical Met-to-Semi transmittance ratio for freestanding 200-nm-thick plain VO_2 film without Ag layer, calculated with Fresnel equations and no fitting parameters. Note: In (b), horizontal axis is in terms of λ_{peak} for M2S-ratio and λ_{vac} for Fresnel-ratio, instead of P_{array}, to facilitate direct comparison. For the fully perforated Ag + VO_2 bilayer in (a), maximum M2S-ratio = 12 at P_{array} = 690 nm and λ_{peak} = 720 nm; for the half-perforated Ag–PlainVO_2 bilayer in (b), M2S-ratio < 1 for all P_{array} and λ_{peak}.

OSA CONTINUUM

that hole arrays in gold + VO_2 and silver + VO_2 bilayer films behave equivalently with regard to EOT modulation effected by the phase transition of the VO_2 layer. Furthermore, comparing Fig. 10(a) to Fig. 4(a) and Fig. 11(a) to Fig. S2(b), along with other simulations not shown here, demonstrates that the glass substrate does not affect the EOT switching.

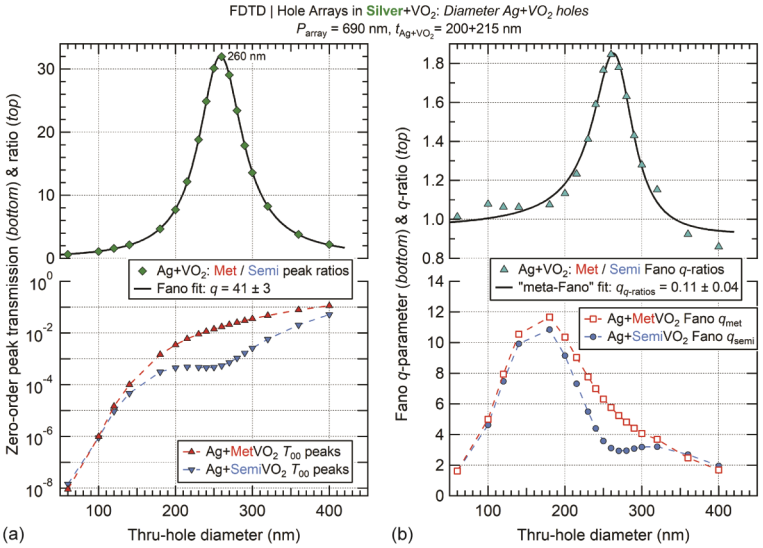

Fig. 11. FDTD simulations of freestanding Ag + VO_2 hole arrays in air. **(a)** Varying thru-hole diameter ($D_{thru-hole} \equiv D_{Ag+VO2} = 60–400$ nm) at fixed period (690 nm), Ag-layer thickness (200 nm) and optimal VO_2-layer thickness (215 nm): (bottom panel) Peak-T_{00} values in $MetVO_2$ and $SemiVO_2$ phases, spanning $\lambda_{peak} = 705–772$ nm wavelength range; (top panel, diamonds) M2S-ratios and (line) Fano-profile fit with Fano parameter $q_{M2S} = 41$, using generalized form of Eq. (1). **(b)** Fano q-parameters extracted from Eq. (1) fits to FDTD T_{00} spectra for different array periods and thru-hole diameters ($P_{array} = 3D_{thru-hole} = 510–1200$ nm): (bottom panel) q_{met} vs. q_{semi}; (top panel, triangles) q_{met}/q_{semi} ratios and (line) "meta-Fano" fit with "meta-Fano" parameter $q_{q-ratios} = 0.11$, using generalized form of Eq. (1). The "valley" around $D_{thru-hole} = 260$ nm in the $SemiVO_2$ curve in (b, bottom) results from changes in the relative contributions to the zero-order transmission of the resonant and non-resonant channels.

An interesting case is presented in Fig. 10(b). The bottom panel shows the peak-T_{00} curves in the $SemiVO_2$ and $MetVO_2$ states of a *half*-perforated freestanding Air-Ag–PlainVO_2-Air hole array, which has holes only in the Ag layer while the VO_2 layer is unperforated ("plain"). [Note: The peak-T_{00} points and corresponding M2S-ratios are plotted as a function of λ_{peak} rather than P_{array}, but the conversion is largely linear, as seen in the inset in Fig. 10(a).] In comparison with the fully perforated Ag + VO_2 hole arrays [Fig. 10(a), bottom panel], the $SemiVO_2$ peak-T_{00} curve of the Ag–PlainVO_2 hole arrays lacks a pronounced "valley" and the $MetVO_2$ curve rises at first but then decreases for $\lambda_{peak} > 720$ nm. The simulated M2S-ratios (square markers) are plotted in Fig. 10(b, top panel), together with an analytical curve (solid line) calculated with the Fresnel equations as a Met-to-Semi ratio of normal-incidence transmittance through a 200-nm-thick VO_2 film without holes and without an Ag overlayer. (Note: The "Fresnel-ratio" curve is plotted as a function of λ_{vac} rather than P_{array} because there are no EOT peaks in the case of a stand-alone plain VO_2 film.) The fact that the M2S-ratio (square markers) of the perforated Ag film sitting on a plain VO_2 film resembles so closely the Fresnel-ratio of the plain VO_2 film alone means that the holes in the VO_2 layer play a critical role in the mechanism responsible for the reverse-switching EOT modulation. Without holes in the VO_2 layer of the bilayer structure, the plasmonic layer (Ag

OSA CONTINUUM

or Au) becomes superfluous for optical switching as the unperforated VO_2 film can modulate the transmitted light just as effectively on its own. Only when the VO_2 layer is also perforated with hole arrays do FP-like resonant effects emerge and enhance the EOT modulation, as described in the preceding sections.

4.10. Varying thru-hole diameter for Air-Ag + VO_2-Air hole arrays

Optimization III(Ag): max(M2S-ratio) = 32 at $\lambda_{peak} = 727$ nm and $D_{thru-hole} = 260$ nm.

We wrap up the optimization sequence with another example of Fano-like behavior [Eq. (1)], this time relating to freestanding Ag + VO_2 hole arrays in air as a function of $D_{thru-hole}$ ($\equiv D_{Ag+VO2} = D_{Ag} = D_{VO2}$). The results plotted in Fig. 11(a) are indeed similar to those in Fig. S2(b) for Au + VO_2 hole arrays on glass. A Fano-profile curve [Fig. 11(a, top panel), solid line) fits the M2S-ratios very well, although the Fano parameter $q_{M2S} = 41$ is rather large, signifying that the asymmetry is low and the M2S-ratio peak has a nearly-Lorentzian shape. On the other hand, Fig. 11(b, bottom panel) shows the Fano parameters in each VO_2 state, extracted from the best-fit Fano profiles of the same EOT spectra represented in Fig. 11(a), while Fig. 11(b, top panel) plots the Met-to-Semi ratios of these q-parameters (triangle markers) as well as a "meta-Fano" fit (solid line)—i.e., a Fano-profile curve fitted to a ratio of Fano parameters. Although this fit is not as good as the one in Fig. 11(a), it yields a "meta" $q_{q-ratios} = 0.11$ that corresponds to a more pronounced asymmetry.

The "valley" in the SemiVO_2 q-parameter curve Fig. 11(b, bottom panel) occurs near $D_{thru-hole} = 260$ nm, which is where in Fig. 11(a) the M2S-ratio has its maximum (top panel) and the SemiVO_2 peak-T_{00} has its "valley" (bottom panel). Recalling that the Fano parameter characterizes the ratio of resonant (discrete) to continuum (direct, non-resonant) contributions to the transmission, the q-parameter curve for SemiVO_2 apparently encodes some changes, relative to the MetVO_2 state, in the coupling strengths of and/or interferences between the resonant and non-resonant transmission channels. The nature of these changes is beyond the scope of the current work, although we are intrigued by the resemblance between the Fano-parameter curve of our Ag + SemiVO_2 hole arrays in Fig. 11(b, bottom panel) and the Fano-parameter curve of Au hole arrays in Fig. 7(c) in Ref. [79].

5. Simulation results: 2D plots of power flow and electric-field intensity

The purpose of this section is to visualize the funneling vs. spreading of optical energy into, respectively, the holes and the xy-plane of the VO_2 layer. It shows several representative 2D color images of the *intensity*, E^2, i.e., the square of the magnitude (`norm` in COMSOL) of the electric field, which is directly proportional to the wave's irradiance. The image plots are overlain with arrows of the time-averaged real part of the Poynting vector, i.e., the *power flow*, $\langle \mathbf{S} \rangle$. The lengths of the $\langle \mathbf{S} \rangle$ arrows are logarithmically scaled in units of W/m^2. Except for Fig. 12, the E^2 colors and $\langle \mathbf{S} \rangle$ arrows are plotted in the two orthogonal half-planes of symmetry that cut through the center of the hole: xz-plane of polarization parallel to the incident wave's electric-field vector $\mathbf{E_{inc}}$, and yz-plane perpendicular to the incident polarization.

In each part of Fig. 12, four xy-plane projections plus the two above-mentioned xz- and yz-plane projections display the *magnitude of the power flow*, $|\langle \mathbf{S} \rangle|$, normalized by the initial irradiance at the input port, I_0 = (Power in)/(Port area), which injects 1 W of power into an area of $(P_{array}/2)^2$. The logarithmic color scale represents $|\langle \mathbf{S} \rangle|/I_0$ as a unitless quantity in dB and is the same in Fig. 12(a, b, c, d): dark blue corresponds to –39 dB, yellow to - 9 dB, and dark red to + 11 dB. Additionally, Fig. 12 delineates the 3D ¼-geometry used in the FEM simulations.

In Fig. 13, Fig. S4 and Fig. S5, E^2 is normalized by $E_0{}^2 = (377\ \text{V/m})^2$, the squared magnitude of the input port's incident electric field. The $E^2/E_0{}^2$ ratios are also plotted as unitless quantities in dB, on *another* consistent logarithmic color scale where dark blue corresponds to + 30 dB, yellow to + 90 dB, and dark red to + 130 dB.

OSA CONTINUUM

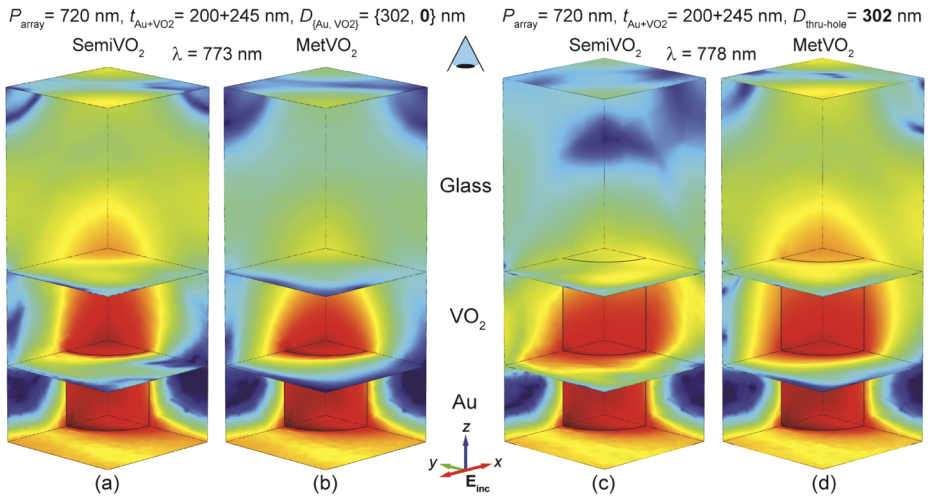

Fig. 12. FEM images of magnitude of power flow in dB, $10\log_{10}(|\langle \mathbf{S} \rangle|/I_0)$, where $\langle \mathbf{S} \rangle$ is time-averaged real part of Poynting vector and I_0 is incident irradiance at input port in W/m^2, for Au + VO_2 hole arrays on glass **(a, b)** without or **(c, d)** with holes in VO_2 layer. Array period (720 nm), Au-hole diameter (302 nm), Au-layer thickness (200 nm) and VO_2-layer thickness (245 nm) are identical for both cases. Illumination source is x-polarized plane wave ($\mathbf{E_{inc}} \parallel \hat{\mathbf{i}}$) injecting 1 W at normal incidence from air medium (not shown) in upward z-direction. Color scale ranges from dark blue (–39 dB) to yellow (–9 dB) to dark red (+11 dB) and represents power flow in xz- and yz-planes of symmetry bounding simulated ¼-cylinder hole, in three xy-planes at Air-Au, Au-VO_2 and VO_2-Glass interfaces, and in xy-plane of detector (top) port. Half-perforated structures without holes in "plain" VO_2 layer (P_{array} = 720 nm, D_{Au} = 302 nm, D_{VO2} = 0 nm, t_{VO2} = 245 nm), in the **(a)** SemiVO_2 and **(b)** MetVO_2 phases, displayed at MetVO_2 peak-T_{00} wavelength (λ_{peak} = 773 nm) [see also Fig. 7(b)]. **(c, d)** Same geometry but with thru-holes perforating both Au and VO_2 layers ($D_{thru-hole} = D_{VO2} = D_{Au}$ = 302 nm) [see also Fig. 6(c)]. Comparing (a) vs. (b), less light spreads into the plane of the unperforated SemiVO_2 layer and more light enters the glass (detector) medium. For (c) vs. (d), the situation is reversed, with higher power flowing through the holes in the MetVO_2 layer and into the glass medium towards the detector port.

5.1. *Unperforated vs. perforated VO_2 layer*

The images in Fig. 12 compare the power-flow magnitude in different planes of the half-perforated Air-Gold–PlainVO_2-Glass hole array (i.e., no holes in the VO_2 layer) [Fig. 12(a, b); see also Fig. 7(b)] vs. the "gold standard" fully perforated Air-Gold + VO_2-Glass hole array [Fig. 12(c, d); see also Fig. 6(c)], in each state of the VO_2 material. Considering the half-perforated case, the power flow spreads farther into the PlainVO_2 layer in the metallic state [Fig. 12(b)] than it does in the semiconducting state [Fig. 12(a)]. Consequently, more detector-bound light enters the glass substrate from the plain SemiVO_2 layer and M2S-ratio = 0.45 < 1 [see Fig. 7(a, top panel, diamonds)]. In the fully perforated, fully optimized case, the situation is reversed: The power flow is relatively more concentrated ("funneled") within the hole in the MetVO_2 state [Fig. 12(d)] than in the SemiVO_2 state [Fig. 12(c)]. Therefore, more light enters the glass substrate in the metallic state and M2S-ratio = 188 >> 1 [see Fig. 6(a, top panel, circles)].

OSA CONTINUUM

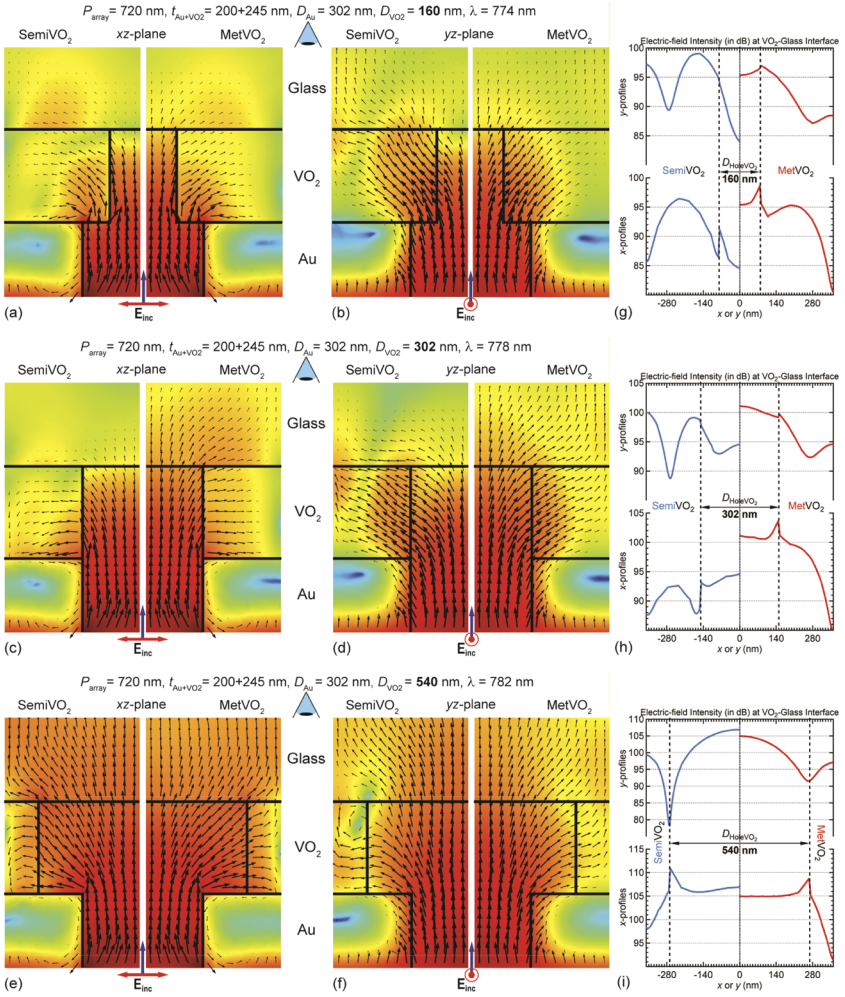

Fig. 13. FEM images of electric-field intensity in dB, 20 $\log_{10}(E/E_0)$, where E_0 is incident electric field at input port, with superimposed arrows of power flow $\langle \mathbf{S} \rangle$ in W/m^2, for Au + VO_2 hole arrays on glass with three different diameters of VO_2-layer holes ($D_{(Hole)VO2}$). Array period (720 nm), Au-hole diameter (302 nm), Au-layer thickness (200 nm) and VO_2-layer thickness (245 nm) are identical for the three cases. Illumination source is *x*-polarized plane wave ($\mathbf{E_{inc}} \,||\, \hat{\mathbf{i}}$) injected from air medium (not shown) at normal incidence in upward z-direction. Color scale ranges from dark blue (+30 dB) to yellow (+90 dB) to dark red (+130 dB) and represents intensity in *xz*- and *yz*-planes of symmetry bounding simulated ¼-cylinder hole (see Fig. 12). Left panel of each subfigure shows half of unit cell cross section in $SemiVO_2$ phase; right panel mirrors same geometry but in $MetVO_2$ phase. Plots for each D_{VO2} value in (*xz, yz*)-planes: **(a, b)** 160 nm, at λ_{peak} = 774 nm [see also Fig. 7(c)]; **(c, d)** 302 nm, at λ_{peak} = 778 nm [see also Fig. 6(c)]; and **(e, f)** 540 nm, at λ_{peak} = 782 nm [see also Fig. 7(e)]. Intensity line profiles for each image in (bottom panels) *x*-direction and (top panels) *y*-direction along VO_2-Glass interface (z = 245 nm), with vertical dashed lines marking VO_2-hole boundaries, extracted from: **(g)** (a, b); **(h)** (c, d); and **(i)** (e, f). Distinguishing features of the intensity in the $SemiVO_2$ state, esp. in the y-profiles, are the spatially sharp dips around y = –270 nm, which belong to patterns reminiscent of standing waves.

OSA CONTINUUM

5.2. Diameter of hole in VO_2 layer

Varying only D_{VO2} (also labeled $D_{HoleVO2}$) while holding the other geometrical parameters constant, was discussed in Section 4.5 and Fig. 7. The plots in Fig. 13 compare the electric-field intensity and power flow for Air-Au + VO_2-Glass hole arrays of three different D_{VO2} values.

When $D_{VO2} = 160\,\text{nm} < D_{Au} = 302\,\text{nm}$ [Fig. 13(a, b, g)], there is almost no EOT modulation since M2S-ratio = 1.01 at $\lambda_{peak} = 774\,\text{nm}$ [see Fig. 7(a, top panel, diamonds) and Fig. 7(c)]. The intensity images (Fig. 13) in the SemiVO_2 state (left panels) look qualitatively similar to their MetVO_2 counterparts (right panels), with two exceptions: (i) a region of relatively low (greenish) intensity localized at the SemiVO_2 output aperture in Fig. 13(a, b); and (ii) a spatially sharp dip in the SemiVO_2 intensity, followed by recovery, at the VO_2-Glass interface about 1/3 of the way in from the left edge in Fig. 13(b). These features are clearly observed in the intensity line profiles extracted along the VO_2-Glass interface: feature (i) spans the regions $-150\,\text{nm} < x < 0\,\text{nm}$ in Fig. 13(g, lower panel) and $-80\,\text{nm} < y < 0\,\text{nm}$ in Fig. 13(g, upper panel); and feature (ii) appears around $y = -270\,\text{nm}$ in Fig. 13(g, upper panel). Although the MetVO_2 y-profile intensity in Fig. 13(g, upper panel) drops even lower than the SemiVO_2 intensity around $y = 265$–$280\,\text{nm}$, the dip is not as sharp as feature (ii) and the MetVO_2 intensity does not recover. A cautionary lesson can be drawn from Fig. 13(g) in conjunction with Fig. 7(c), namely that the relative light intensities registered at the output apertures of the bilayer hole array do not always predict the relative amounts of T_{00} reaching the far field in the two VO_2 phases. To state the obvious, the VO_2 material *between* the holes plays a critical role in the EOT modulation.

The intensity images [Fig. 13(c, d)] and line profiles [Fig. 13(h)] for $D_{VO2} = 302\,\text{nm} = D_{Au}$ qualitatively resemble those described above, but there is clearly a much higher overall intensity above this MetVO_2 layer, as seen in the upper right regions of the right panels of Fig. 13(c, d), in comparison with the same regions above the SemiVO_2 layer (left panels). It was shown in Section 4.4 that this so-dubbed "gold standard" geometric configuration has one of the highest (non-hypothetical) switching ratios, M2S-ratios = 188 [see Fig. 6(a, c)], so it is not surprising that the holes in the MetVO_2 layer appear to better funnel the light through than the holes in the SemiVO_2 layer—in other words, with less "leakage" into the bulk of the VO_2 film [cf. left vs. right panels in Fig. 13(c, d)]. Interestingly, the sharp dip in the SemiVO_2 intensity around $y = -270\,\text{nm}$ [Fig. 13(h, upper panel)] is a narrower and deeper version of the same feature described above in the case of $D_{VO2} = 160\,\text{nm}$ [Fig. 13(g, upper panel)].

At $D_{VO2} = 540\,\text{nm} > D_{Au} = 302\,\text{nm}$, the holes in the VO_2 layer are, to a first approximation, no longer subwavelength since the cutoff diameter below which waveguiding in a cylindrical hole in a perfect electric conductor becomes evanescent [79] would be $D_c = \lambda_{peak}/1.71 = 457\,\text{nm} < 540\,\text{nm}$. Because most of the light emerging from the holes in the Au layer then propagates through the empty (air) space of the holes in the VO_2 layer [Fig. 13(e, f)], the interaction with the VO_2 material is relatively weak and so is the EOT modulation: M2S-ratio = 0.90 at $\lambda_{peak} = 782\,\text{nm}$ [see Fig. 7(a, e)]. The intensity images [Fig. 13(e, f)] and line profiles [Fig. 13(i)] look quite similar in the two VO_2 phases—again except for the dip in the SemiVO_2 intensity around $y = -270\,\text{nm}$, now even sharper [Fig. 13(i, upper panel)]. In this particular case, the dip spatially coincides with the rim of the SemiVO_2 hole. The origin of this persistent intensity dip is unclear; it may belong to a lateral (xy-plane) resonance generated at the Au-VO_2 interface for the Au-hole diameter ($D_{Au} = 302\,\text{nm}$) common to the three cases discussed above.

5.3. Thickness of VO_2 layer

(See Supplement 1 for content.)

5.4. Array period with scaled thru-hole diameter

(See Supplement 1 for content.)

OSA CONTINUUM

6. Summary

We have performed FDTD and FEM electromagnetic simulations and preliminary experiments in order to optimize the geometry of bilayer gold + VO_2 and silver + VO_2 nanohole arrays towards a large modulation of the zero-order optical transmission within narrow spectral bands. The highest feasible switching ratio obtained in the simulations is close to 200, which makes such perforated bilayer structures potentially useful for high-speed tunable switching [93,94] of optical signals in hybrid nanophotonic-nanoplasmonic devices. For example, the relative spectral purity, deep modulation and ultrafast phase transition of the bilayer hole array may make it a competitive component of active display technologies based on plasmonic structural colors [28]. In the course of the optimization process, we uncovered Fabry-Perot and Fano (anti-)resonances for variations of individual geometrical and optical parameters. The resonances appear to be coupled: for example, changing the periodicity of the hole array also affects the value of the VO_2 film thickness that maximizes the switching ratio. The FP-type anti-resonances arise from the peculiar index of refraction of semiconducting VO_2 in the 600–1000 nm wavelength range, where the real part has a nearly non-dispersive value (~3) and the extinction coefficient is small (~0.4) and also nearly constant. The simulations have mapped the parameter space of the bilayer hole arrays and are currently guiding more extensive experiments to test the robustness of the EOT modulation against real-world fabrication and measurement conditions.

Funding

Office of Science (CNMS2018-161, CNMS2019-171).

Acknowledgments

E. U. Donev gratefully acknowledges the expert support of ORNL/CNMS staff scientists Christopher Rouleau, Jason Fowlkes, Dayrl Briggs and Dale Hensley. Fabrication of some of the VO_2 thin films was conducted at the Center for Nanophase Materials Sciences (CNMS2018-161, CNMS2019-171), which is a DOE Office of Science User Facility.

Disclosures

The authors declare no conflicts of interest.

See Supplement 1 for supporting content.

References

1. W. L. Barnes, A. Dereux, and T. W. Ebbesen, "Surface plasmon subwavelength optics," Nature **424**(6950), 824–830 (2003).
2. F. J. G. de Abajo, "Colloquium: Light scattering by particle and hole arrays," Rev. Mod. Phys. **79**(4), 1267–1290 (2007).
3. C. Genet and T. W. Ebbesen, "Light in tiny holes," Nature **445**(7123), 39–46 (2007).
4. F. J. Garcia-Vidal, L. Martin-Moreno, T. W. Ebbesen, and L. Kuipers, "Light passing through subwavelength apertures," Rev. Mod. Phys. **82**(1), 729–787 (2010).
5. N. C. Lindquist, P. Nagpal, K. M. McPeak, D. J. Norris, and S.-H. Oh, "Engineering metallic nanostructures for plasmonics and nanophotonics," Rep. Prog. Phys. **75**(3), 036501 (2012).
6. H. Bethe, "Theory of diffraction by small holes," Phys. Rev. **66**(7-8), 163–182 (1944).
7. C. J. Bouwkamp, "Theoretical and Numerical Treatment of Diffraction through a Circular Aperture," IRE Trans. Antennas Propag. **18**(2), 152–176 (1970).
8. J. V. Coe, J. M. Heer, S. Teeters-Kennedy, H. Tian, and K. R. Rodriguez, "Extraordinary Transmission of Metal Films with Arrays of Subwavelength Holes," Annu. Rev. Phys. Chem. **59**(1), 179–202 (2008).
9. P. Lalanne and H. Liu, "A New Look at Grating Theories Through the Extraordinary Optical Transmission Phenomenon," in *Plasmonics: From Basics to Advanced Topics*, 167S. Enoch and N. Bonod, eds. (Springer Berlin Heidelberg, Berlin, Heidelberg, 2012), pp. 85–103.

OSA CONTINUUM

10. S. G. Rodrigo, F. d. León-Pérez, and L. Martín-Moreno, "Extraordinary Optical Transmission: Fundamentals and Applications," Proc. IEEE **104**(12), 2288–2306 (2016).
11. H. Liu and P. Lalanne, "Comprehensive microscopic model of the extraordinary optical transmission," J. Opt. Soc. Am. A **27**(12), 2542–2550 (2010).
12. X. Zhang, H. Liu, and Y. Zhong, "Microscopic analysis of surface Bloch modes on periodically perforated metallic surfaces and their relation to extraordinary optical transmission," Phys. Rev. B **89**(19), 195431 (2014).
13. S. A. Darmanyan and A. V. Zayats, "Light tunneling via resonant surface plasmon polariton states and the enhanced transmission of periodically nanostructured metal films: An analytical study," Phys. Rev. B **67**(3), 035424 (2003).
14. W. L. Barnes, "Surface plasmon-polariton length scales: a route to sub-wavelength optics," J. Opt. A: Pure Appl. Opt. **8**(4), S87–S93 (2006).
15. F. van Beijnum, C. Retif, C. B. Smiet, H. Liu, P. Lalanne, and M. P. van Exter, "Quasi-cylindrical wave contribution in experiments on extraordinary optical transmission," Nature **492**(7429), 411–414 (2012).
16. A. Y. Nikitin, S. G. Rodrigo, F. J. García-Vidal, and L. Martín-Moreno, "In the diffraction shadow: Norton waves versus surface plasmon polaritons in the optical region," New J. Phys. **11**(12), 123020 (2009).
17. R. Gordon, A. G. Brolo, D. Sinton, and K. L. Kavanagh, "Resonant optical transmission through hole-arrays in metal films: physics and applications," Laser Photonics Rev. **4**(2), 311–335 (2010).
18. A.-P. Blanchard-Dionne and M. Meunier, "Sensing with periodic nanohole arrays," Adv. Opt. Photonics **9**(4), 891–940 (2017).
19. A. Prasad, J. Choi, Z. Jia, S. Park, and M. R. Gartia, "Nanohole array plasmonic biosensors: Emerging point-of-care applications," Biosens. Bioelectron. **130**, 185–203 (2019).
20. B. Ai, Z. Wang, H. Möhwald, and G. Zhang, "Plasmonic Nanochemistry Based on Nanohole Array," ACS Nano **11**(12), 12094–12102 (2017).
21. M. L. Juan, M. Righini, and R. Quidant, "Plasmon nano-optical tweezers," Nat. Photonics **5**(6), 349–356 (2011).
22. C. Escobedo, A. G. Brolo, R. Gordon, and D. Sinton, "Optofluidic concentration: plasmonic nanostructure as concentrator and sensor," Nano Lett. **12**(3), 1592–1596 (2012).
23. D. Tordera, D. Zhao, A. V. Volkov, X. Crispin, and M. P. Jonsson, "Thermoplasmonic Semitransparent Nanohole Electrodes," Nano Lett. **17**(5), 3145–3151 (2017).
24. Q. Yu, S. Braswell, B. Christin, J. Xu, P. M. Wallace, H. Gong, and D. Kaminsky, "Surface-enhanced Raman scattering on gold quasi-3D nanostructure and 2D nanohole arrays," Nanotechnology **21**(35), 355301 (2010).
25. L. E. G. Armas, J. W. Menezes, M. G. Huila, K. Araki, and H. E. Toma, "Gold Nanohole Arrays Fabricated by Interference Lithography Technique as SERS Probes for Chemical Species Such As Rhodamine 6G and 4,4′-Bipyridine," Plasmonics **12**(4), 1015–1020 (2017).
26. A. Mahigir, T.-W. Chang, A. Behnam, G. L. Liu, M. R. Gartia, and G. Veronis, "Plasmonic nanohole array for enhancing the SERS signal of a single layer of graphene in water," Sci. Rep. **7**(1), 14044 (2017).
27. A. Kristensen, J. K. W. Yang, S. I. Bozhevolnyi, S. Link, P. Nordlander, N. J. Halas, and N. A. Mortensen, "Plasmonic colour generation," Nat. Rev. Mater. **2**(1), 16088 (2017).
28. K. Xiong, D. Tordera, M. P. Jonsson, and A. B. Dahlin, "Active control of plasmonic colors: emerging display technologies," Rep. Prog. Phys. **82**(2), 024501 (2019).
29. F. van Beijnum, P. J. van Veldhoven, E. J. Geluk, M. J. de Dood, G. W. t'Hooft, and M. P. van Exter, "Surface plasmon lasing observed in metal hole arrays," Phys. Rev. Lett. **110**(20), 206802 (2013).
30. A. Djalalian-Assl, J. J. Cadusch, E. Balaur, and M. Aramesh, "Tunable surface plasmon wave plates," Opt. Lett. **41**(13), 3146–3148 (2016).
31. E. Hendry, M. J. Lockyear, J. Gómez Rivas, L. Kuipers, and M. Bonn, "Ultrafast optical switching of the THz transmission through metallic subwavelength hole arrays," Phys. Rev. B **75**(23), 235305 (2007).
32. S. P. Palto, Y. A. Draginda, V. V. Artemov, and M. V. Gorkunov, "Optical control of plasmonic grating transmission by photoinduced anisotropy," J. Opt. **19**(7), 074001 (2017).
33. A. Kumar, Y. K. Srivastava, M. Manjappa, and R. Singh, "Color-Sensitive Ultrafast Optical Modulation and Switching of Terahertz Plasmonic Devices," Adv. Opt. Mater. **6**(15), 1800030 (2018).
34. T. T. Hoang, Q. M. Ngo, D. L. Vu, and H. P. T. Nguyen, "Controlling Fano resonances in multilayer dielectric gratings towards optical bistable devices," Sci. Rep. **8**(1), 16404 (2018).
35. R. Sahin, "Control of EOT on sub-wavelength Au hole arrays via Fano resonances," Opt. Commun. **454**, 124431 (2020).
36. A. Battula, S. Chen, Y. Lu, R. J. Knize, and K. Reinhardt, "Tuning the extraordinary optical transmission through subwavelength hole array by applying a magnetic field," Opt. Lett. **32**(18), 2692–2694 (2007).
37. K. Bi, W. Liu, Y. Guo, G. Dong, and M. Lei, "Magnetically tunable broadband transmission through a single small aperture," Sci. Rep. **5**(1), 12489 (2015).
38. E. A. Shaner, J. G. Cederberg, and D. Wasserman, "Electrically tunable extraordinary optical transmission gratings," Appl. Phys. Lett. **91**(18), 181110 (2007).
39. T. J. Kim, T. Thio, T. W. Ebbesen, D. E. Grupp, and H. J. Lezec, "Control of optical transmission through metals perforated with subwavelength hole arrays," Opt. Lett. **24**(4), 256–258 (1999).
40. W. Dickson, G. A. Wurtz, P. R. Evans, R. J. Pollard, and A. V. Zayats, "Electronically Controlled Surface Plasmon Dispersion and Optical Transmission through Metallic Hole Arrays Using Liquid Crystal," Nano Lett. **8**(1), 281–286 (2008).

OSA CONTINUUM

41. S. Kim, M. S. Jang, V. W. Brar, Y. Tolstova, K. W. Mauser, and H. A. Atwater, "Electronically tunable extraordinary optical transmission in graphene plasmonic ribbons coupled to subwavelength metallic slit arrays," Nat. Commun. **7**(1), 12323 (2016).
42. M. Atighilorestani, D. P. dos Santos, R. F. V. V. Jaimes, M. M. Rahman, M. L. A. Temperini, and A. G. Brolo, "Electrochemical Control of Light Transmission through Nanohole Electrode Arrays," ACS Photonics **3**(12), 2375–2382 (2016).
43. K. Xiong, D. Tordera, G. Emilsson, O. Olsson, U. Linderhed, M. P. Jonsson, and A. B. Dahlin, "Switchable Plasmonic Metasurfaces with High Chromaticity Containing Only Abundant Metals," Nano Lett. **17**(11), 7033–7039 (2017).
44. J. Y. Suh, E. U. Donev, R. Lopez, L. C. Feldman, and R. F. Haglund, "Modulated optical transmission of subwavelength hole arrays in metal-VO_2 films," Appl. Phys. Lett. **88**(13), 133115 (2006).
45. E. U. Donev, J. Y. Suh, F. Villegas, R. Lopez, R. F. Haglund, and L. C. Feldman, "Optical properties of subwavelength hole arrays in vanadium dioxide thin films," Phys. Rev. B **73**(20), 201401 (2006).
46. J. Jeong, A. Joushaghani, S. Paradis, D. Alain, and J. K. S. Poon, "Electrically controllable extraordinary optical transmission in gold gratings on vanadium dioxide," Opt. Lett. **40**(19), 4408–4411 (2015).
47. M. Sun, M. Taha, S. Walia, M. Bhaskaran, S. Sriram, W. Shieh, and R. R. Unnithan, "A Photonic Switch Based on a Hybrid Combination of Metallic Nanoholes and Phase-change Vanadium Dioxide," Sci. Rep. **8**(1), 11106 (2018).
48. F. J. Morin, "Oxides which show a metal-to-insulator transition at the Neel temperature," Phys. Rev. Lett. **3**(1), 34–36 (1959).
49. Z. Shao, X. Cao, H. Luo, and P. Jin, "Recent progress in the phase-transition mechanism and modulation of vanadium dioxide materials," NPG Asia Mater. **10**(7), 581–605 (2018).
50. Y. Ke, S. Wang, G. Liu, M. Li, T. J. White, and Y. Long, "Vanadium Dioxide: The Multistimuli Responsive Material and Its Applications," Small **14**(39), 1802025 (2018).
51. Z. Yang, C. Y. Ko, and S. Ramanathan, "Oxide electronics utilizing ultrafast metal-insulator transitions," Annu. Rev. Mater. Res. **41**(1), 337–367 (2011).
52. D. Y. Lei, K. Appavoo, F. Ligmajer, Y. Sonnefraud, R. F. Haglund, and S. A. Maier, "Optically-Triggered Nanoscale Memory Effect in a Hybrid Plasmonic-Phase Changing Nanostructure," ACS Photonics **2**(9), 1306–1313 (2015).
53. T. Jostmeier, M. Mangold, J. Zimmer, H. Karl, H. J. Krenner, C. Ruppert, and M. Betz, "Thermochromic modulation of surface plasmon polaritons in vanadium dioxide nanocomposites," Opt. Express **24**(15), 17321–17331 (2016).
54. L. Liu, L. Kang, T. S. Mayer, and D. H. Werner, "Hybrid metamaterials for electrically triggered multifunctional control," Nat. Commun. **7**(1), 13236 (2016).
55. S. K. Earl, T. D. James, D. E. Gómez, R. E. Marvel, R. F. Haglund, and A. Roberts, "Switchable polarization rotation of visible light using a plasmonic metasurface," APL Photonics **2**(1), 016103 (2017).
56. S.-J. Kim, H. Yun, K. Park, J. Hong, J.-G. Yun, K. Lee, J. Kim, S. J. Jeong, S.-E. Mun, J. Sung, Y. W. Lee, and B. Lee, "Active directional switching of surface plasmon polaritons using a phase transition material," Sci. Rep. **7**(1), 43723 (2017).
57. N. A. Butakov, I. Valmianski, T. Lewi, C. Urban, Z. Ren, A. A. Mikhailovsky, S. D. Wilson, I. K. Schuller, and J. A. Schuller, "Switchable Plasmonic–Dielectric Resonators with Metal–Insulator Transitions," ACS Photonics **5**(2), 371–377 (2018).
58. N. Kumar, A. Rúa, J. Aldama, K. Echeverría, F. E. Fernández, and S. Lysenko, "Photoinduced surface plasmon switching at VO_2/Au interface," Opt. Express **26**(11), 13773–13782 (2018).
59. H. W. Verleur, A. S. Barker, and C. N. Berglund, "Optical Properties of VO_2 between 0.25 and 5 eV," Phys. Rev. **172**(3), 788–798 (1968).
60. J. B. K. Kana, J. M. Ndjaka, G. Vignaud, A. Gibaud, and M. Maaza, "Thermally tunable optical constants of vanadium dioxide thin films measured by spectroscopic ellipsometry," Opt. Commun. **284**(3), 807–812 (2011).
61. K. Dai, J. Lian, M. J. Miller, J. Wang, Y. Shi, Y. Liu, H. Song, and X. Wang, "Optical properties of VO2 thin films deposited on different glass substrates," Opt. Mater. Express **9**(2), 663–672 (2019).
62. E. U. Donev, J. Y. Suh, R. Lopez, L. C. Feldman, and R. F. Haglund, "Using a Semiconductor-to-Metal Transition to Control Optical Transmission through Subwavelength Hole Arrays," Adv. OptoElectron. **2008**, 739135 (2008).
63. B. Hou, J. Mei, M. Ke, W. Wen, Z. Liu, J. Shi, and P. Sheng, "Tuning Fabry-Perot resonances via diffraction evanescent waves," Phys. Rev. B **76**(5), 054303 (2007).
64. R. Filter, J. Qi, C. Rockstuhl, and F. Lederer, "Circular optical nanoantennas: an analytical theory," Phys. Rev. B **85**(12), 125429 (2012).
65. C.-P. Huang and C.-T. Chan, "Deep subwavelength Fabry-Perot resonances," EPJ Appl. Metamat. **1**, 2 (2014).
66. C. Genet, M. P. van Exter, and J. P. Woerdman, "Fano-type interpretation of red shifts and red tails in hole array transmission spectra," Opt. Commun. **225**(4-6), 331–336 (2003).
67. M. Sarrazin, J. P. Vigneron, and J. M. Vigoureux, "Role of Wood anomalies in optical properties of thin metallic films with a bidimensional array of subwavelength holes," Phys. Rev. B **67**(8), 085415 (2003).
68. E. S. H. Kang, H. Ekinge, and M. P. Jonsson, "Plasmonic fanoholes: on the gradual transition from suppressed to enhanced optical transmission through nanohole arrays in metal films of increasing film thickness," Opt. Mater. Express **9**(3), 1404–1415 (2019).
69. J. Y. Suh, R. Lopez, L. C. Feldman, and R. F. Haglund, "Semiconductor to metal phase transition in the nucleation and growth of VO_2 nanoparticles and thin films," J. Appl. Phys. **96**(2), 1209–1213 (2004).

OSA CONTINUUM

70. A. V. Lavrinenko, J. Lægsgaard, N. Gregersen, F. Schmidt, and T. Søndergaard, *Numerical Methods in Photonics* (CRC Press, 2014).
71. A. Taflove and S. C. Hagness, *Computational Electrodynamics: The Finite-difference Time-domain Method* (Artech House, 2005).
72. A. Z. Elsherbeni and V. Demir, *The Finite-difference Time-domain Method for Electromagnetics with MATLAB Simulations* (SciTech Pub., 2009).
73. Y. Kane, "Numerical solution of initial boundary value problems involving maxwell's equations in isotropic media," IEEE Trans. Antennas Propag. **14**(3), 302–307 (1966).
74. P. B. Johnson and R. W. Christy, "Optical constants of the noble metals," Phys. Rev. B **6**(12), 4370–4379 (1972).
75. H. Liu and P. Lalanne, "Microscopic theory of the extraordinary optical transmission," Nature **452**(7188), 728–731 (2008).
76. W. Dai and C. M. Soukoulis, "Theoretical analysis of the surface wave along a metal-dielectric interface," Phys. Rev. B **80**(15), 155407 (2009).
77. S.-H. Chang, S. K. Gray, and G. C. Schatz, "Surface plasmon generation and light transmission by isolated nanoholes and arrays of nanoholes in thin metal films," Opt. Express **13**(8), 3150–3165 (2005).
78. J. Bravo-Abad, L. Martín-Moreno, F. J. García-Vidal, E. Hendry, and J. Gómez Rivas, "Transmission of light through periodic arrays of square holes: From a metallic wire mesh to an array of tiny holes," Phys. Rev. B **76**(24), 241102 (2007).
79. E. Laux, C. Genet, and T. W. Ebbesen, "Enhanced optical transmission at the cutoff transition," Opt. Express **17**(9), 6920–6930 (2009).
80. J.-B. Masson, A. Podzorov, and G. Gallot, "Extended Fano model of Extraordinary Electromagnetic Transmission through subwavelength hole arrays in the terahertz domain," Opt. Express **17**(17), 15280–15291 (2009).
81. A. Hajebifard and P. Berini, "Fano resonances in plasmonic heptamer nano-hole arrays," Opt. Express **25**(16), 18566–18580 (2017).
82. U. Fano, "Effects of Configuration Interaction on Intensities and Phase Shifts," Phys. Rev. **124**(6), 1866–1878 (1961).
83. B. Luk'yanchuk, N. I. Zheludev, S. A. Maier, N. J. Halas, P. Nordlander, H. Giessen, and C. T. Chong, "The Fano resonance in plasmonic nanostructures and metamaterials," Nat. Mater. **9**(9), 707–715 (2010).
84. M. F. Limonov, M. V. Rybin, A. N. Poddubny, and Y. S. Kivshar, "Fano resonances in photonics," Nat. Photonics **11**(9), 543–554 (2017).
85. A. Degiron and T. W. Ebbesen, "The role of localized surface plasmon modes in the enhanced transmission of periodic subwavelength apertures," J. Opt. A: Pure Appl. Opt. **7**(2), S90–S96 (2005).
86. J. W. Yoon and R. Magnusson, "Fano resonance formula for lossy two-port systems," Opt. Express **21**(15), 17751–17759 (2013).
87. C. Ott, A. Kaldun, P. Raith, K. Meyer, M. Laux, J. Evers, C. H. Keitel, C. H. Greene, and T. Pfeifer, "Lorentz Meets Fano in Spectral Line Shapes: A Universal Phase and Its Laser Control," Science **340**(6133), 716–720 (2013).
88. S. G. Rodrigo, "Extraordinary Optical Transmission," in *Optical Properties of Nanostructured Metallic Systems: Studied with the Finite-Difference Time-Domain Method*, S. G. Rodrigo, ed. (Springer Berlin Heidelberg, 2012), pp. 37–75.
89. V. Giannini, Y. Francescato, H. Amrania, C. C. Phillips, and S. A. Maier, "Fano Resonances in Nanoscale Plasmonic Systems: A Parameter-Free Modeling Approach," Nano Lett. **11**(7), 2835–2840 (2011).
90. H. F. Ghaemi, T. Thio, D. E. Grupp, T. W. Ebbesen, and H. J. Lezec, "Surface plasmons enhance optical transmission through subwavelength holes," Phys. Rev. B **58**(11), 6779–6782 (1998).
91. K. L. van der Molen, F. B. Segerink, N. F. van Hulst, and L. Kuipers, "Influence of hole size on the extraordinary transmission through subwavelength hole arrays," Appl. Phys. Lett. **85**(19), 4316–4318 (2004).
92. J. S. Toll, "Causality and the Dispersion Relation: Logical Foundations," Phys. Rev. **104**(6), 1760–1770 (1956).
93. A. Cavalleri, C. Tóth, C. W. Siders, J. A. Squier, F. Ráksi, P. Forget, and J. C. Kieffer, "Femtosecond Structural Dynamics in VO_2 during an Ultrafast Solid-Solid Phase Transition," Phys. Rev. Lett. **87**(23), 237401 (2001).
94. Y. Zhou, X. Chen, C. Ko, Z. Yang, C. Mouli, and S. Ramanathan, "Voltage-Triggered Ultrafast Phase Transition in Vanadium Dioxide Switches," IEEE Electron Device Lett. **34**(2), 220–222 (2013).